Unconditionally Stable Sequential Schemes for All-way Coupled Thermoporomechanics: Undrained-Adiabatic and Extended Fixed-Stress Splits

Jihoon Kim[a]

[a]*Department of Petroleum Engineering, Texas A&M University, Richardson Bldg., 3116 TAMU College Station, TX 77843-3116, USA*

Abstract

We propose two sequential methods for the all-way coupled thermoporomechanical problems: the undrained-adiabatic split that combines together the undrained and adiabatic methods of poromechanics and thermomechanics, respectively, and the extended fixed-stress split. We perform nonlinear stability analysis for the two sequential methods, introducing a new extended norm that can encompass the all-way coupled thermoporomechanical problems. We find that the two sequential methods are unconditionally stable if $\alpha \geq 0.5$, where α is the parameter of time discretization for the generalized midpoint rule at $t_{n+\alpha}$. We also perform the spectral analysis in order to further investigate stability and convergence of the two methods. The spectral analysis shows unconditional stability of the two sequential methods, which yields the magnitudes of the amplification factor less than unity. We then show numerical examples, which support the a priori stability and convergence estimates.

Keywords: Thermoporomechanics, Sequential Scheme, Stability analysis, Unconditional stability

1. Introduction

Coupled heat, fluid flow, and mechanics, called thermoporomechanics, are currently of much interest in many areas of geosciences and reservoir engineering to model complex physics. For example, in geothermal engineering, heat energy is delivered to flowing fluid, which transports heat to the surface facilities by fluid production [1]. Heat increases fluid temperature, which changes pore-pressure and other physical variables such as fluid phases. In turn, the changes in pore-pressure or temperature affect stress of the porous media, which causes deformation and surface subsidence [2, 3]. In the gas hydrate bearing sediments, changes in stress and temperature fields influence gas hydrate formation or dissociation. This might cause well instability or possible methane emission to the surface due to geological failure [4, 5]. In the case of in-situ conversion and steam injection for heavy oil production, thermal behavior plays a critical role in hydrocarbon production. Freezing the boundary walls and injecting heat to the production wells may cause substantial surface subsidence, which can support the reservoir pressure by compaction. The changes in stress and strain fields induce different fluid-heat flow regimes.

Nuclear waste disposal to the underground requires accurate modeling of thermoporomechanics [6]. Radioactive materials generate heat, which can perturb an initial stable condition, causing fluid flow or reservoir deformation.

Email address: jihoon.kim@tamu.edu (Jihoon Kim)

Petrophysical properties can be affected by the changes in the effective stress and/or temperature directly [7]. Frost heaving in cold climate areas damages water-infiltrated materials [8]. The phase change between liquid water and ice induces the change in density, which leads to pore-volume change, followed by deformation and possibly material failure. This physical behavior is similar to the physics in the gas hydrate sediments during formation and dissociation of gas hydrate [4]. For all the above cases, accurate and rigorous modeling for thermoporomechanics is necessary because individual physics such as fluid, heat, and geomechanics are tightly coupled.

In numerical modeling, there are two solution strategies to solve the coupled problems: monolithic and sequential (staggered) approaches [9, 10]. The monolithic approach can typically provide numerical stability for well-posed problems. However, it requires high computational cost and code development of a unified non-isothermal fluid flow-mechanics simulator in solving thermoporomechanics. Furthermore, an appropriate preconditioning method for the full Jacobian matrix is another challenging issue on the monolithic method, when we take the Newton-Raphson method. On the other hand, the staggered approach, also called the fractional step method, is desirable when we make use of the existing robust simulators, because an appropriate interface code between the simulators is required only, reducing coding effort. In addition, the staggered approach can be modified straightforwardly for preconditioning the full Jacobian matrix of the monolithic method [11]. However, it should be noted that staggered methods may be limited by numerical stability [9, 12]. Thus, finding staggered methods that can yield numerical stability and accuracy is a critical issue in solving coupled problems.

Several studies have considerably been done in order to find unconditionally stable staggered methods. For example, Armero and Simo [9, 13] proposed the adiabatic split for thermomechanics. Later, for poromechanics, Armero [14] extended the undrained split, originally proposed by Zienkiewicz et al. [15], to nonlinear mechanics. By the undrained (or adiabatic) split, mechanics is solved at the first step with no fluid (or heat) flow, and then fluid (or heat) flow is solved after solution of mechanics. These splitting methods keep thermodynamic stability, and can provide unconditional numerical stability. The thermodynamically consistent time integration is known to be very robust [16]. Kim et al. [17], Kim et al. [18], and Mikelic and Wheeler [19] investigated stability and convergence of poromechanics for four staggered methods (drained, undrained, fixed-strain, fixed-stress). By the fixed strain (or stress) method, we solve fluid flow at the first step, fixing stain (or stress) fields, and then mechanics is solved after solution of flow. They found that the drained and fixed-strain method, obvious operator splitting methods, are only conditionally stable, and that their instability cannot be fixed by reducing time step size. Even though the undrained method is unconditionally stable, it may be inaccurate when the coupling strength is high. On the other hand, the fixed-stress method is unconditionally stable and accurate even for high coupling strength. Then, Kim et al. [20] and Kim et al. [3] applied the fixed-stress method to gas hydrate and geothermal systems, while assuming no direct heat generation from solid deformation. In other words, they considered two-way coupling between fluid flow and geomechanics, while one-way coupling from heat flow (i.e., energy equation) to geomechanics was used. Large heat capacity and/or the small thermal coupling coefficient, falls in most Earth science problems, can justify neglecting the term of no direct heat generation from deformation in heat flow.

Yet, in some cases such as large heat generation due to friction between well casings and reservoir formations or

fault slip, the effects from direct heat generation of geomechanics might not be ignorable, and all-way coupling among fluid flow, heat flow, and geomechanics can provide better accuracy. For example, Liu et al. [21] employed the all-way coupling in thermoporomechanics in order to model complex physics near the wellbore. The sequential scheme might be more pragmatic for large scale problems of thermoporomechanics in reservoir simulation.

With this motivation in mind, we investigate unconditionally stable staggered methods for all-way coupled thermoporomechanical problems. We first propose a staggered method that combines the undrained split of poromechanics with the adiabatic split of thermomechanics, named *undrained-adiabatic split*. Another sequential method to be studied in this paper is namely the *extended fixed-stress split*. In this method, the numerical relaxation terms and the corresponding correction terms are applied to not only fluid flow (i.e., mass conservation equation) but also heat flow (i.e., energy equation), accounting for the direct heat contribution coming from deformation to heat flow. It should be noted that stability analyses of the previous studies cannot encompass the sequential methods proposed in this study, because the norms used in the previous studies cannot encompass the all-way coupled thermoporomechanical problems. Hence, we will perform new stability analysis for the undrained-adiabatic and extended fixed-stress split methods, introducing a new extended norm for nonlinear stability analysis. We will show that the two sequential methods are unconditionally stable (i.e., B-stable), when $\alpha \geq 0.5$. Furthermore, we will also perform the spectral analysis for the linear (linearized) coupled systems in order to find more specific properties of stability and convergence of the two methods. We will show numerical examples, which support the a-priori mathematical estimates.

2. Mathematical formulation

We employ a classical continuum representation, where fluid and solid are viewed as overlapping continua [22]. The governing equation for multiphase fluid flow comes from mass balance as follows.

$$\frac{dm_J}{dt} + \mathrm{Div}\, \boldsymbol{w}_J = (\rho f)_J \,, \tag{1}$$

where $\boldsymbol{w}_J$ is the mass flux of fluid phase J (mass flow rate per unit area) relative to the solid skeleton. dm_J/dt is the variation of fluid mass relative to the solid skeleton. We denote by $\frac{d(\cdot)}{dt}$ the change of a physical quantity $(\cdot)$ relative to the solid skeleton. ρ_J is the density of fluid phase J, and f_J is a volumetric source term of phase J.

For mechanics, the quasi-static assumption yields the governing equation as

$$\mathrm{Div}\, \boldsymbol{\sigma} + \rho_b \boldsymbol{g} = \boldsymbol{0}, \tag{2}$$

where $\mathrm{Div}(\cdot)$ is the divergence operator, $\boldsymbol{\sigma}$ is the Cauchy total-stress tensor, $\boldsymbol{g}$ is the gravity vector, $\rho_b = \phi\rho_f + (1-\phi)\rho_s$ is the bulk density, ρ_f is total fluid density, ρ_s is the density of the solid phase, and ϕ is the true porosity. The true porosity is defined as the ratio of the pore volume to the bulk volume in the deformed configuration. Tensile stress is positive. In this paper, we assume small deformation (i.e., infinitesimal transformation).

The energy equation (heat flow) can be driven by the second law of thermodynamics, i.e., entropy balance, expressed as [23]

$$T\left(\frac{d\bar{S}}{dt} + \mathrm{Div}(\bar{s}_J \boldsymbol{w}_J)\right) = -\,\mathrm{Div}(\boldsymbol{q}) + \Phi_M + Q_s, \tag{3}$$

where $\bar{S}$ is the total entropy, $\bar{s}_J$ is the internal entropy per unit mass of phase J (i.e., specific entropy), and Φ_M is the mechanical dissipation. Repeated subscripts imply summation. $\boldsymbol{q}$ is the heat flow vector by conduction. Q_s is the external heat source term. Taking the assumption that the viscous dissipation is negligible (i.e., the Brinkman number is very low), Equation 3 can be rewritten as [23]

$$T\left(\frac{d\bar{S}}{dt} - \bar{s}_J \frac{dm_J}{dt}\right) = -\operatorname{Div}(\boldsymbol{q}) - \underbrace{C_{p,J}\boldsymbol{w}_J}_{\boldsymbol{v}_T} \cdot \mathbf{Grad}\, T + Q_s, \tag{4}$$

where T is temperature. $C_{p,J}$ is the volumetric specific heat capacity at constant pressure for fluid phase J. At the right side of Equation 4, the first and second terms correspond to the heat conduction and convection, respectively. The left term is the heat accumulation term, which will be described by the constitutive relations more specifically.

Coussy [22] considers the first and second laws of thermodynamics, and applies them to the Clausius-Duhem inequality. Then, taking the hypothesis that all intrinsic, mass flow, and heat conduction dissipations are non-negative, the constitutive relations in thermoporoelasticity are obtained as

$$\delta\boldsymbol{\sigma} = \mathbf{C}_{dr} : \delta\boldsymbol{\varepsilon} - b_J \delta p_J \mathbf{1} - 3\alpha_T K_{dr} \delta T \mathbf{1}, \tag{5}$$

$$\left(\frac{\delta m}{\rho}\right)_J = b_J \delta\varepsilon_v + N_{JK}\delta p_K - 3\alpha_{m,J}\delta T, \tag{6}$$

$$\delta\bar{S} = \bar{s}_J \delta m_J + 3\alpha_T K_{dr}\delta\boldsymbol{\varepsilon}_v - 3\alpha_{m,J}\delta p_J + \underbrace{\frac{C_d}{T}}_{C_d^*}\delta T, \tag{7}$$

where $\mathbf{C}_{dr}$ is the drained-isothermal elastic moduli, $\mathbf{N} = \{N_{JK}\}$ is the inverse matrix of the Biot moduli $\mathbf{M} = \{M_{JK}\}$ (i.e., $\mathbf{N} = \mathbf{M}^{-1}$), where $\mathbf{N}$ and $\mathbf{M}$ are positive definite. b_J takes $b_J = bS_J$, where b is the Biot coefficient in single phase flow and S_J is saturation of phase J. $3\alpha_T$ is the volumetric skeleton thermal dilation coefficient, K_{dr} is the drained isothermal bulk modulus, $\mathbf{1}$ is the rank-2 identity tensor, ε_v is the total volumetric strain, and $3\alpha_{m,J} = 3\alpha_\phi + \phi 3\alpha_J$, where $3\alpha_\phi$ and $3\alpha_J$ are the coefficients of thermal dilation related to porosity and fluid J, respectively. $C_d = C_{sk} + m_J C_{p,J}$ is the total volumetric heat capacity, where C_{sk} is the volumetric heat capacity of the solid skeleton. 'δ' implies the variation relative to the motion of solid skeleton. The fluid volume flux relative to the motion of the solid skeleton, $\boldsymbol{v}_J = (\boldsymbol{w}/\rho)_J$, is given by Darcy's law as

$$\boldsymbol{v}_J = -\boldsymbol{k}_{p,JK}(\mathbf{Grad}\, p_K - \rho_K \boldsymbol{g}), \tag{8}$$

where $\boldsymbol{k}_{p,JK}$ is the symmetric positively definite effective permeability tensor for phases J and K, in which fluid phase viscosity μ_J is taken into account. The thermal conduction is expressed by Fourier's laws as

$$\boldsymbol{q} = -\boldsymbol{k}_T\, \mathbf{Grad}\, T, \tag{9}$$

where $\boldsymbol{k}_T$ is the symmetric positively definite thermal conductivity tensor.

Substituting Equations 5 – 9 into Equations 1, 2, and 4, the governing equations are expressed by the fluid pressure, strain, and temperature, which will be the primary variables for numerical simulation. For mathematical completeness, we specify initial and boundary conditions. For fluid flow we consider the boundary conditions $p_J = \bar{p}_J$ (prescribed pressure) on Γ_p, and $\boldsymbol{v}_J \cdot \boldsymbol{n} = \bar{v}_J$ (prescribed volumetric flux) on Γ_v, where $\boldsymbol{n}$ is the outward unit normal to the boundary, $\partial\Omega$. For well-posedness of the problem, we assume that $\Gamma_p \cap \Gamma_v = \emptyset$, and $\Gamma_p \cup \Gamma_v = \partial\Omega$. For heat flow we consider the boundary conditions $T = \bar{T}$ (prescribed pressure) on Γ_T, and $\boldsymbol{f}_T \cdot \boldsymbol{n} = \bar{f}_T$ (prescribed volumetric heat flux) on Γ_{f_T} We assume that $\Gamma_T \cap \Gamma_{f_T}\emptyset$, and $\Gamma_T \cup \Gamma_{f_T} = \partial\Omega$. The boundary conditions for the mechanical problem are $\boldsymbol{u} = \bar{\boldsymbol{u}}$ (prescribed displacement) on Γ_u and $\boldsymbol{\sigma} \cdot \boldsymbol{n} = \bar{\boldsymbol{t}}$ (prescribed traction) on Γ_σ. Again, we assume $\Gamma_u \cap \Gamma_\sigma = \emptyset$, and $\Gamma_u \cup \Gamma_\sigma = \partial\Omega$. For plasticity, we can easily extend the constitutive relation by introducing hardening variables and forces [22, 24].

3. Discretization

For space discretization, the finite-volume method for fluid and heat flow is widely used in reservoir flow simulation [25] while the nodal-based finite-element method for mechanics is typically used in the geotechnical and mechanical engineering [26, 15, 27, 28, 9, 14, 29, 30]. For the fluid and heat flow problems, the pressure and temperature are located at the cell center, while the displacement vector is located at vertices for the mechanical problem. The pressure and displacement take the piecewise-constant and piecewise-linear interpolations, respectively. This space discretization strategy has the following characteristics: local mass and heat conservation at the element level, a continuous displacement field, which allows for tracking the deformation, and convergent approximations with the lowest-order discretization.

The given space discretization provides a stable pressure field, while the finite-element methods can cause spurious pressure oscillations if equal-order approximations of pressure and displacement (e.g., piecewise continuous interpolation) are used [31, 32, 33]. Specifically, the piecewise-linear and piecewise-constant approximation of displacement and pressure, typically called Q1-P0 discretization, does not fully satisfy the inf-sup condition, which may cause the checker board pressure oscillation [26]. However, the Q1-P0 discretization with the fixed stress method can overcome the pressure oscillation, being considered as a type of the stabilized Uzawa iteration for the saddle point problem, even for the cases that the Q1-P0 with the direct solver causes the pressure oscillation [34].

We obtain a fully discrete system of equations by further discretizing in time the accumulation terms in fluid flow and energy equations. In this study, the generalized midpoint rule is used for time discretization [35].

4. Sequential methods for thermoporomechanics

The fully implicit method solves Equations 1, 2, and 4 simultaneously by using the Newton-Raphson method, while sequential methods split those equations into two or more subproblems and solve them sequentially. In this study, we propose and study the undrained-adiabatic and extended fixed-stress splits for thermoporomechanics as follows.

4.1. Undrained-adiabatic split

Motivated by Armero and Simo [9] in thermoelasticity and by Zienkiewicz et al. [15] and Armero [14] in isothermal poroelasticity and poroelastoplasticity, the undrained-adiabatic split freezes fluid mass and heat variation when mechanics is solved at the first step (i.e., $\delta m_J = 0$ and $\delta \bar{S} = 0$). Thus, the undrained-adiabatic split decomposes the original problem into

$$\begin{bmatrix} \boldsymbol{u}^n \\ \boldsymbol{p}_J^n \\ T^n \end{bmatrix} \xrightarrow{\mathcal{A}_{ua}^u} \begin{bmatrix} \boldsymbol{u}^{n+1} \\ \boldsymbol{p}_J^* \\ T^* \end{bmatrix} \xrightarrow{\mathcal{A}_{ua}^{fl}} \begin{bmatrix} \boldsymbol{u}^{n+1} \\ \boldsymbol{p}_J^{n+1} \\ T^{n+1} \end{bmatrix}, \quad \text{where} \quad \begin{cases} \mathcal{A}_{ua}^u : \operatorname{Div} \boldsymbol{\sigma} + \rho_b \boldsymbol{g} = \boldsymbol{0},\ \delta m_J = 0,\ \delta \bar{S} = 0, \\ \mathcal{A}_{ua}^{fl} : \begin{cases} \dot{m}_J + \operatorname{Div} \boldsymbol{w}_J = (\rho f)_J, \\ T\left(\dot{\bar{S}} - \bar{s}_J \dot{m}_J\right) = -\operatorname{Div}(\boldsymbol{q}) - \boldsymbol{v}_T \cdot \mathbf{Grad}\, T + Q_s, \\ \dot{\boldsymbol{\varepsilon}} : \text{prescribed}, \end{cases} \end{cases} \tag{10}$$

where $(\cdot)_{ua}$ stands for the undrained-adiabatic split. The intermediate pressure and temperature, p_J^* and T^*, can be calculated locally and explicitly after we obtain the displacement, $\boldsymbol{u}^{n+1}$. The superscript n denotes time level t_n. From Equations 6 and 7, the constraints $\delta m_J = 0$ and $\delta \bar{S} = 0$ yield

$$\delta p_J = M_{JK}\left(-b_K - \frac{9\alpha_{m,K}}{C_{ud}^*}\left(\alpha_T K_{dr} + \alpha_{m,J} M_{JL} b_L\right)\right)\delta\varepsilon_v, \tag{11}$$

$$\delta T = -\frac{3\alpha_T K_{dr} + 3\alpha_{m,J} M_{JL} b_L}{C_{ud}^*}\delta\varepsilon_v, \tag{12}$$

where

$$C_{ud}^* = \frac{C_{ud}}{T},\ C_{ud} = C_d - 9\alpha_{m,J} M_{JK} \alpha_{m,K} T, \tag{13}$$

in which C_{ud} is the undrained iso-deformation heat capacity.

Remark 1. C_{ud}^* is *non-negative* for wellposedness. Thus, $C_d \geq 9\alpha_{m,J} M_{JK} \alpha_{m,K} T$.

Using Equations 11 and 12, the total stress of mechanics can be expressed at the discrete level as

$$\boldsymbol{\sigma}^{n+1} - \boldsymbol{\sigma}^n = \mathbf{C}_{ud}^{ad} : \left(\boldsymbol{\varepsilon}^{n+1} - \boldsymbol{\varepsilon}^n\right), \tag{14}$$

where $\mathbf{C}_{ud}^{ad}$ is the undrained-adiabatic elastic moduli written as

$$\mathbf{C}_{ua} = \mathbf{C}_{dr} + \left(b_J M_{JK} b_K + \frac{9\left(\alpha_T K_{dr} + \alpha_{m,J} M_{JK} b_K\right)^2}{C_d^{ud}}\right)\mathbf{1} \otimes \mathbf{1}. \tag{15}$$

After solving mechanics with the undrained-adiabatic moduli, we solve fluid and heat flow with the mechanics solutions obtained at the mechanics step.

4.2. Extended-fixed-stress split

The extended fixed-stress split solves the fluid and heat flow problems simultaneously at the first step fixing the rate of the total stress (i.e., $\delta\dot{\boldsymbol{\sigma}} = \mathbf{0}$). The fixed-stress approach splits the original problem as follows:

$$\begin{bmatrix} \boldsymbol{u}^n \\ \boldsymbol{p}_J^n \\ T^n \end{bmatrix} \xrightarrow{\mathcal{A}_{ss}^{fl}} \begin{bmatrix} \boldsymbol{u}^* \\ \boldsymbol{p}_J^{n+1} \\ T^{n+1} \end{bmatrix} \xrightarrow{\mathcal{A}_{ss}^{u}} \begin{bmatrix} \boldsymbol{u}^{n+1} \\ \boldsymbol{p}_J^{n+1} \\ T^{n+1} \end{bmatrix}, \quad \text{where} \quad \begin{cases} \mathcal{A}_{ss}^{fl}: & \begin{cases} \dot{m}_J + \operatorname{Div} \boldsymbol{w}_J = (\rho f)_J, \\ T\left(\dot{\bar{S}} - \bar{s}_J \dot{m}_J\right) = -\operatorname{Div}(\boldsymbol{q}) - \boldsymbol{v}_T \cdot \mathbf{Grad}\, T + Q_s, \\ \delta\dot{\boldsymbol{\sigma}} = 0, \end{cases} \\ \mathcal{A}_{ss}^{u}: \operatorname{Div} \boldsymbol{\sigma} + \rho_b \boldsymbol{g} = \mathbf{0},\ (p_J,\, T): \text{prescribed}, \end{cases} \tag{16}$$

where the subscript $(\cdot)_{ss}$ stands for the extended-fixed-stress split. The initial condition of the flow problem, $\mathcal{A}_{ss}^{fl}$, is specified from the original coupled problem that satisfies

$$\operatorname{Div} \dot{\sigma}_{t=0} = 0\,, \quad \operatorname{Div} \sigma_{t=0} + \rho_b \boldsymbol{g} = 0. \tag{17}$$

In this scheme, the mean (volumetric) total stress terms in the accumulation terms of the fluid and heat flow problems are evaluated explicitly at the flow step as follows.

$$\left(\frac{\Delta m^n}{\rho}\right)_J = \frac{b_J}{K_{dr}} \Delta\sigma_v^{n-1} + \left(N_{JK} + \frac{b_J b_K}{K_{dr}}\right) \Delta p_K^n - 3\left(\alpha_{m,J} - b_J \alpha_T\right) \Delta T^n, \tag{18}$$

$$T\left(\Delta S^n - s_J \Delta m_J^n\right) = 3T\alpha_T \Delta\sigma_v^{n-1} - 3T\left(\alpha_{m,J} - \alpha_T b_J\right) \Delta p_J^n + T\left(C_d^* + 9\alpha_T^2 K_{dr}\right) \Delta T^n, \tag{19}$$

where $\Delta(\cdot)^n = (\cdot)^{n+1} - (\cdot)^n$. The total mean stress term can be also expressed by the primary variables as

$$\Delta {\sigma_v}^{n-1} = K_{dr} \Delta\varepsilon_v^{n-1} - b_J \Delta p_J^{n-1} - 3\alpha_T K_{dr} \Delta T^{n-1}. \tag{20}$$

After the step of fluid and heat flow, we solve mechanics with the updated pressure and temperature.

Remark 2. The first term of the right side in Equation 19 (i.e., $3T\alpha_T \Delta\sigma_v^{n-1}$) is the correction term from solution of the geomechanics problem in heat flow, which can consider the two-way coupling between geomechanics and heat flow. Additionally, compared with Equations 6 and 7, $\frac{b_J b_K}{K_{dr}}$ and $b_J \alpha_T$ of fluid flow (Equation 18) are considered as relaxation terms for numerical stability. $\alpha_T b_J$ and $9\alpha_T^2 K_{dr}$ of heat flow (Equation 18) are also the terms of numerical stability.

5. Dissipative character of thermoporomechanics and numerical stability of the monolithic method

Consider the domain Ω at an equilibrium condition where $\boldsymbol{\varepsilon}_0$, $p_{J,0}$ and T_0 are strain, fluid phase pressure, and temperature in equilibrium, respectively. Suppose we have an initial perturbation in the limited domain Ω^p inside the boundary (i.e., $\Omega^p \subset \Omega$), as shown in Figure 1. Then, we investigate the evolution of the perturbation in time with the homogeneous governing equations as

$$\begin{aligned} \operatorname{Div} {}^d\boldsymbol{\sigma} &= \mathbf{0}, \\ {}^d\dot{m}_{J,} + \operatorname{Div} {}^d\boldsymbol{w}_J &= 0, \\ {}^dT\left({}^d\dot{\bar{S}} - \bar{s}_J {}^d\dot{m}_J\right) &= -\operatorname{Div}({}^d\boldsymbol{q}) - {}^d\boldsymbol{v}_T \cdot \mathbf{Grad}\, {}^dT \end{aligned} \tag{21}$$

where the homogeneous boundary conditions are applied, because we have no perturbation at the boundary, Γ. The subscript ${}^{d}(\cdot)$ implies the perturbed variables. This concept is fundamentally same as the thermodynamic stability discussed in Coussy [22]. In Equation 4, we approximate the convection term ${}^{d}\boldsymbol{v}_T \cdot \mathbf{Grad}\, {}^{d}T$ as

$$ {}^{d}\boldsymbol{v}_T \cdot \mathbf{Grad}\, {}^{d}T \approx \mathrm{Div}({}^{d}\boldsymbol{v}_T {}^{d}T), \tag{22} $$

assuming $\mathrm{Div}\, {}^{d}\boldsymbol{v}_T {}^{d}T << \mathbf{Grad}\, {}^{d}T \cdot {}^{d}\boldsymbol{v}_T$. Using Equation 22, the right side of Equation 3 can expressed as

$$ \mathrm{Div}({}^{d}\boldsymbol{q}) + {}^{d}\boldsymbol{v}_T \cdot \mathbf{Grad}\, {}^{d}T \approx \mathrm{Div}\, \underbrace{({}^{d}\boldsymbol{q} + {}^{d}\boldsymbol{v}_T {}^{d}T)}_{{}^{d}\boldsymbol{f}_T}, \tag{23} $$

where $\boldsymbol{f}_T$ is the heat flux. Equation 23 is employed in Liu et al. [21]. On the other hand, when we perform the spectral analysis later, we keep the original form $\boldsymbol{v}_T \cdot \mathbf{Grad}\, T$ in Equation 4.

Note that, due to the homogeneous boundary conditions, we have

$$ \int_\Gamma {}^{d}\boldsymbol{f}_T \cdot d\Gamma = 0. \tag{24} $$

Also, since ${}^{d}\boldsymbol{\varepsilon}$, ${}^{d}p_J$ and ${}^{d}T$ satisfy the constitutive relations of Equations 5 – 7, we have

$$ \begin{aligned} {}^{d}\boldsymbol{\sigma} &= \mathbf{C}_{dr} : {}^{d}\boldsymbol{\varepsilon} - b_J {}^{d}p_J \mathbf{1} - 3\alpha_T K_{dr} {}^{d}T \mathbf{1}, && (25)\\ \left(\frac{{}^{d}m}{\rho}\right)_J &= b_J {}^{d}\varepsilon_v + N_{JK} {}^{d}p_K - 3\alpha_{m,J} {}^{d}T, && (26)\\ {}^{d}\bar{S} &= \bar{s}_J {}^{d}m_J + 3\alpha_T K_{dr} {}^{d}\boldsymbol{\varepsilon}_v - 3\alpha_{m,J} {}^{d}p_J + C_d^{*d}T. && (27) \end{aligned} $$

In elasticity, we employ a norm extended from isothermal poromechanics to thermoporomechanics, as

$$ \begin{aligned} \|\chi\|_{\mathcal{N}}^2 &= \frac{1}{2}\int_\Omega \left(\boldsymbol{\varepsilon} : \mathbf{C}_{dr}\boldsymbol{\varepsilon} + \left(\left(\frac{m}{\rho}\right)_J - b_J\varepsilon_v\right) M_{JK} \left(\left(\frac{m}{\rho}\right)_K - b_K\varepsilon_v\right) + C_{ud}^* T^2\right) d\Omega, && (28)\\ \mathcal{N} &:= \left\{\chi := (\boldsymbol{\varepsilon}, m_J, T) \in \mathbb{S}\times\mathbb{R}^{\mathrm{n_p}}\times\mathbb{R} :\ \varepsilon_{ij} \in L^2(\Omega),\ m_J \in L^2(\Omega),\ T \in L^2(\Omega)\right\}, \end{aligned} $$

where $\mathbb{S} = \mathbb{R}^{(n_{\mathrm{dim}}+1)n_{\mathrm{dim}}/2}$ is the vector space of symmetric rank-two tensors, in which n_{dim} is the dimension of the domain Ω^0. n_p is the number of fluid phase. Let us introduce the norms associated for sub-problems, as follows.

$$ \begin{aligned} \|\boldsymbol{\varepsilon}\|_{\mathcal{E}}^2 &= \frac{1}{2}\int_\Omega \boldsymbol{\varepsilon} : \mathbf{C}_{dr}\boldsymbol{\varepsilon} d\Omega,\ \ \mathcal{E} := \left\{\boldsymbol{\varepsilon} \in \mathbb{S} :\ \varepsilon_{ij} \in L^2(\Omega),\right\}, && (29)\\ \|\boldsymbol{\kappa}\|_{\mathcal{M}}^2 &= \frac{1}{2}\int_\Omega \kappa_J M_{JK} \kappa_K d\Omega,\ \ \mathcal{M} := \left\{\boldsymbol{\kappa} \in \mathbb{R}^{\mathrm{n_p}} :\ \kappa_J \in L^2(\Omega)\right\},\ \ \boldsymbol{\kappa} = \left(\left(\frac{m}{\rho}\right)_J - b_J\varepsilon_v\right), && (30)\\ \|T\|_{\mathcal{T}}^2 &= \frac{1}{2}\int_\Omega C_{ud}^* T^2 d\Omega,\ \ \mathcal{T} := \left\{T \in \mathbb{R} :\ T \in L^2(\Omega)\right\}, && (31) \end{aligned} $$

from which we have

$$\|\chi\|^2_{\mathcal{N}} = \|\boldsymbol{\varepsilon}\|^2_{\mathcal{E}} + \|\boldsymbol{\kappa}\|^2_{\mathcal{M}} + \|T\|^2_{\mathcal{T}}\,. \tag{32}$$

Then, we show the dissipative character of the all-way thermoporomechanics problem, relative to the norms, $\|\cdot\|_{\mathcal{N}}$ as follows.

$$\begin{aligned}
\frac{d\left\|{}^d\chi\right\|^2_{\mathcal{N}}}{dt} &= \frac{\partial\left\|{}^d\chi\right\|^2_{\mathcal{N}}}{\partial {}^d\boldsymbol{\varepsilon}} : {}^d\dot{\boldsymbol{\varepsilon}} + \frac{\partial\left\|{}^d\chi\right\|^2_{\mathcal{N}}}{\partial {}^d m_J}\,{}^d\dot{m}_J + \frac{\partial\left\|{}^d\chi\right\|^2_{\mathcal{N}}}{\partial {}^d T}\,{}^d\dot{T} \\
&= \int_\Omega ({}^d\boldsymbol{\sigma}' : {}^d\dot{\boldsymbol{\varepsilon}} + \left(N_{JL}\,{}^d p_L - 3\alpha_{m,J}\,{}^d T\right) M_{JK} \underbrace{\left(\left(\frac{{}^d\dot{m}}{\rho}\right)_K - b_K\,{}^d\dot{\varepsilon}_v\right)}_{=N_{JL}\,{}^d\dot{p}_L - 3\alpha_{m,J}\,{}^d\dot{T}} + C^*_{ud}\,{}^d T\,{}^d\dot{T})d\Omega \\
&= \int_\Omega (\underbrace{{}^d\boldsymbol{\sigma} + b_J\,{}^d p_J\mathbf{1} + 3\alpha_T K_{dr}\,{}^d T\mathbf{1}}_{{}^d\boldsymbol{\sigma}'}) : {}^d\dot{\boldsymbol{\varepsilon}} d\Omega \\
&\quad + \int_\Omega \left(\left(\frac{{}^d p}{\rho}\right)_J {}^d\dot{m}_J - b_J\,{}^d p_J\,{}^d\dot{\boldsymbol{\varepsilon}}_v - 3\alpha_{m,J}\,{}^d T\,{}^d\dot{p}_J + 9\alpha_{m,J} M_{JK}\alpha_{m,K}\,{}^d T\,{}^d\dot{T}\right) d\Omega \\
&\quad + \int_\Omega (\underbrace{{}^d T\,{}^d\dot{S} - {}^d T\bar{s}_J\,{}^d\dot{m}_J - 3\alpha_T K_{dr}\,{}^d T\,{}^d\dot{\boldsymbol{\varepsilon}}_v + 3\alpha_{m,J}\,{}^d T\,{}^d\dot{p}_J}_{C_d\,{}^d\dot{T}} - 9\alpha_{m,J} M_{JK}\alpha_{m,K}\,{}^d T\,{}^d\dot{T})d\Omega \\
&= \int_\Omega \left({}^d\boldsymbol{\sigma} : {}^d\boldsymbol{\varepsilon} + \left(\frac{{}^d p}{\rho}\right)_J {}^d\dot{m}_J + {}^d T\left({}^d\dot{S} - \bar{s}_J\,{}^d\dot{m}_J\right)\right) d\Omega \\
&= \underbrace{\int_\Omega {}^d\boldsymbol{\sigma} : {}^d\dot{\boldsymbol{\varepsilon}} d\Omega}_{=0} - \int_\Omega {}^d p_J \operatorname{Div}({}^d\boldsymbol{v}_J)d\Omega - \int_\Omega \operatorname{Div}{}^d\boldsymbol{f}_T d\Omega \\
&= -\int_\Omega \underbrace{{}^d\boldsymbol{v}_J \cdot \mathbf{k}^{-1}_{p,JK}\,{}^d\boldsymbol{v}_K}_{\geq 0} d\Omega - \underbrace{\int_\Gamma {}^d\boldsymbol{f}_T \cdot n d\Gamma}_{=0} \leq 0,
\end{aligned} \tag{33}$$

where $\boldsymbol{v}_J \in [H(\mathrm{Div}, \Omega)]^{n_{\mathrm{dim}}}$, and the divergence theorem, Darcy's and Fourier's laws are applied. Equation 33 implies that the given mathematical problem is contractive.

At the next step, we investigate numerical stability for the monolithic method by the energy method. Numerical stability can be defined by the algorithmic counter part of the dissipative character, written as

$$\left\|{}^d\chi^{n+1}\right\|_{\mathcal{N}} \leq \left\|{}^d\chi^{n}\right\|_{\mathcal{N}}. \tag{34}$$

As the counter part of the continuum problem, the governing equations at the discrete time level under the generalized midpoint rule are given as

$$\operatorname{Div}{}^d\boldsymbol{\sigma}^{n+\alpha} = \mathbf{0}, \tag{35}$$

$$\Delta^d m_J{}^n = -\Delta t \operatorname{Div}{}^d\boldsymbol{w}^{n+\alpha}_J, \tag{36}$$

$${}^d T^{n+\alpha}\left(\Delta^d \bar{S}^n - \bar{s}^{n+\alpha}_J \Delta^d m_J{}^n\right) = -\Delta t \operatorname{Div}{}^d f^{n+\alpha}_T, \tag{37}$$

where Δt is the time step size. From the generalized midpoint rule, we have $(\cdot)^{n+\alpha} = (1-\alpha)(\cdot)^n + \alpha(\cdot)^{n+1}$, where $0 \leq \alpha \leq 1$. We also consider the following identity equations.

$$\left(\left\|{}^d\boldsymbol{\varepsilon}^{n+1}\right\|_{\mathcal{E}}^2 - \left\|{}^d\boldsymbol{\varepsilon}^{n}\right\|_{\mathcal{E}}^2\right) = \int_\Omega {}^d\boldsymbol{\varepsilon}^{n+\alpha} : \mathbf{C}_{dr}\left({}^d\boldsymbol{\varepsilon}^{n+1} - {}^d\boldsymbol{\varepsilon}^{n}\right) d\Omega - (2\alpha-1)\left\|{}^d\boldsymbol{\varepsilon}^{n+1} - {}^d\boldsymbol{\varepsilon}^{n}\right\|_{\mathcal{E}}^2, \tag{38}$$

$$\left(\left\|{}^d\boldsymbol{\kappa}^{n+1}\right\|_{\mathcal{M}}^2 - \left\|{}^d\boldsymbol{\kappa}^{n}\right\|_{\mathcal{M}}^2\right) = \int_\Omega {}^d\boldsymbol{\kappa}_J^{n+\alpha} M_{JK}({}^d\boldsymbol{\kappa}_K^{n+1} - {}^d\boldsymbol{\kappa}_K^{n}) d\Omega - (2\alpha-1)\left\|{}^d\boldsymbol{\kappa}^{n+1} - {}^d\boldsymbol{\kappa}^{n}\right\|_{\mathcal{M}}^2, \tag{39}$$

$$\left\|{}^dT^{n+1}\right\|_{\mathcal{T}}^2 - \left\|{}^dT^{n}\right\|_{\mathcal{T}}^2 = \int_\Omega {}^dT^{n+\alpha} C_{ud}^*({}^dT^{n+1} - {}^dT^{n}) d\Omega - (2\alpha-1)\left\|{}^dT^{n+1} - {}^dT^{n}\right\|_{\mathcal{T}}^2. \tag{40}$$

For mechanics, Equation 35 satisfies

$$\int_\Omega {}^d\boldsymbol{\sigma}^{n+\alpha} : \Delta^d\boldsymbol{\varepsilon}^n d\Omega = 0, \tag{41}$$

which yields

$$\int_\Omega \underbrace{{}^d\boldsymbol{\sigma}^{n+\alpha\prime}}_{\mathbf{C}_{dr}\,{}^d\boldsymbol{\varepsilon}^{n+\alpha}} : \Delta^d\boldsymbol{\varepsilon}^n d\Omega - \int_\Omega b_J\, {}^dp^{n+\alpha}\Delta^d\boldsymbol{\varepsilon}_v^n d\Omega - \int_\Omega {}^dT^{n+\alpha} 3\alpha_T K_{dr}\Delta^d\boldsymbol{\varepsilon}_v^n d\Omega = 0. \tag{42}$$

Using Equation 38 and 42, we obtain

$$\left(\left\|{}^d\boldsymbol{\varepsilon}^{n+1}\right\|_{\mathcal{E}}^2 - \left\|{}^d\boldsymbol{\varepsilon}^{n}\right\|_{\mathcal{E}}^2\right) = 0 + \int_\Omega \Delta^d\varepsilon_v^n b_J\, {}^dp_J^{n+\alpha} d\Omega + \int_\Omega \Delta^d\varepsilon_v^n 3\alpha_T K_{dr}\, {}^dT^{n+\alpha} d\Omega - (2\alpha-1)\left\|{}^d\boldsymbol{\varepsilon}^{n+1} - {}^d\boldsymbol{\varepsilon}^{n}\right\|_{\mathcal{E}}^2. \tag{43}$$

For fluid flow, Equation 36 satisfies

$$\int_\Omega {}^dp_J^{n+\alpha}\left(\frac{\Delta^d m}{\rho}^n\right)_J d\Omega = -\Delta t \int_\Omega \left(\frac{{}^dp^{n+\alpha}}{\rho}\right)_J \mathrm{Div}\, {}^d\boldsymbol{w}_J^{n+\alpha} d\Omega, \tag{44}$$

which yields

$$\int_\Omega {}^dp_J^{n+\alpha}\left(\frac{\Delta^d m}{\rho}^n\right)_J d\Omega = \Delta t \int_\Gamma \underbrace{{}^dp_J^{n+\alpha}\, {}^d\boldsymbol{v}_J^{n+\alpha}}_{=0} d\Gamma - \Delta t \int_\Omega {}^d\boldsymbol{v}_J^{n+\alpha} \cdot \mathbf{k}_{p,JK}{}^{-1}\, {}^d\boldsymbol{v}^{n+\alpha}{}_K d\Omega, \tag{45}$$

where the integration by parts is applied. Then, we have

$$
\begin{aligned}
&\left(\left\|{}^{d}\boldsymbol{\kappa}^{n+1}\right\|_{\mathcal{M}}^{2}-\left\|{}^{d}\boldsymbol{\kappa}^{n}\right\|_{\mathcal{M}}^{2}\right)\\
&=\int_{\Omega}\underbrace{\left({}^{d}p_{K}-3\alpha_{m,J}M_{JK}{}^{d}T\right)^{n+\alpha}}_{{}^{d}\boldsymbol{\kappa}_{J}{}^{n+\alpha}M_{JK}}\underbrace{(\left(\left(\frac{{}^{d}m^{n+1}}{\rho}\right)_{K}-b_{K}{}^{d}\varepsilon_{v}^{n+1}\right)-\left(\left(\frac{{}^{d}m^{n}}{\rho}\right)_{K}-b_{K}{}^{d}\varepsilon_{v}^{n}\right))}_{\Delta^{d}\boldsymbol{\kappa}_{K}^{n}}d\Omega\\
&\quad-(2\alpha-1)\left\|{}^{d}\boldsymbol{\kappa}^{n+1}-{}^{d}\boldsymbol{\kappa}^{n}\right\|_{\mathcal{M}}^{2},\\
&=\int_{\Omega}{}^{d}p_{K}^{n+\alpha}\left(\frac{\Delta^{d}m^{n}}{\rho}\right)_{K}d\Omega-\int_{\Omega}\Delta^{d}\varepsilon_{v}^{n}b_{J}{}^{d}p_{J}^{n+\alpha}d\Omega-\int_{\Omega}3^{d}T^{n+\alpha}\alpha_{m,J}M_{JK}\underbrace{\left(\left(\frac{{}^{d}\Delta m^{n}}{\rho}\right)_{K}-b_{K}\Delta^{d}\varepsilon_{v}^{n}\right)}_{\Delta^{d}\boldsymbol{\kappa}_{K}^{n}}d\Omega\\
&\quad-(2\alpha-1)\left\|{}^{d}\boldsymbol{\kappa}^{n+1}-{}^{d}\boldsymbol{\kappa}^{n}\right\|_{\mathcal{M}}^{2},\\
&=-\Delta t\underbrace{\int_{\Omega}{}^{d}\boldsymbol{v}_{J}^{n+\alpha}\cdot\mathbf{k}_{p,JK}{}^{-1}{}^{d}\boldsymbol{v}^{n+\alpha}{}_{K}d\Omega}_{\geq 0}-\int_{\Omega}\Delta^{d}\varepsilon_{v}^{n}b_{J}{}^{d}p_{J}^{n+\alpha}d\Omega\\
&\quad-\int_{\Omega}3^{d}T^{n+\alpha}\alpha_{m,J}M_{JK}\left(\left(\frac{\Delta^{d}m^{n}}{\rho}\right)_{K}-b_{K}\Delta^{d}\varepsilon_{v}^{n}\right)d\Omega-(2\alpha-1)\left\|{}^{d}\boldsymbol{\kappa}^{n+1}-{}^{d}\boldsymbol{\kappa}^{n}\right\|_{\mathcal{M}}^{2}.
\end{aligned}
\tag{46}
$$

For heat flow, Equation 37 satisfies

$$
\int_{\Omega}{}^{d}T^{n+\alpha}\left(\Delta^{d}\bar{S}^{n}-\bar{s}_{J}^{n+\alpha}{}^{d}\Delta m_{J}{}^{n}\right)d\Omega=-\Delta t\int_{\Omega}\mathrm{Div}\,{}^{d}\boldsymbol{f}_{T}^{n+\alpha}d\Omega,
\tag{47}
$$

which produces by using the constitutive relations

$$
\begin{aligned}
&\left\|{}^{d}T^{n+1}\right\|_{\mathcal{T}}^{2}-\left\|{}^{d}T^{n}\right\|_{\mathcal{T}}^{2}\\
&=\int_{\Omega}\underbrace{{}^{d}T^{n+\alpha}\overbrace{\left(\Delta^{d}\bar{S}^{n}-\bar{s}_{J}^{n+\alpha}\Delta^{d}m_{J}{}^{n}-3\alpha_{T}K_{dr}\Delta^{d}\varepsilon_{v}^{n}+3\alpha_{m,J}\Delta^{d}p_{J}^{n}\right)}^{C_{d}^{*}\Delta^{d}T^{n}}-9\alpha_{m,J}M_{JK}\alpha_{m,K}{}^{d}T^{n+\alpha}\Delta^{d}T^{n}}_{{}^{d}T^{n+\alpha}C_{ud}^{*}\Delta^{d}T^{n}}d\Omega\\
&\quad-(2\alpha-1)\left\|{}^{d}T^{n+1}-{}^{d}T^{n}\right\|_{\mathcal{T}}^{2}\\
&=-\Delta t\underbrace{\int_{\Gamma}{}^{d}\boldsymbol{f}_{T}^{n+\alpha}\cdot nd\Gamma}_{=0}-\int_{\Omega}\Delta^{d}\varepsilon_{v}^{n}3\alpha_{T}K_{dr}{}^{d}T^{n+\alpha}d\Omega+\int_{\Omega}3^{d}T^{n+\alpha}\alpha_{m,J}M_{JK}\underbrace{\left(\left(\frac{\Delta^{d}m^{n}}{\rho}\right)_{K}-b_{K}\Delta^{d}\varepsilon_{v}^{n}\right)}_{\Delta^{d}\kappa_{K}^{n}}d\Omega\\
&\quad-(2\alpha-1)\left\|{}^{d}T^{n+1}-{}^{d}T^{n}\right\|_{\mathcal{T}}^{2}.
\end{aligned}
\tag{48}
$$

Then, summing Equations 42, 46, and 48, we have

$$
\begin{aligned}
&\left\| {}^{d}\chi^{n+1} \right\|_{\mathcal{N}}^{2} - \left\| {}^{d}\chi^{n} \right\|_{\mathcal{N}}^{2} \\
&= \left(\left\| {}^{d}\boldsymbol{\varepsilon}^{n+1} \right\|_{\mathcal{E}}^{2} - \left\| {}^{d}\boldsymbol{\varepsilon}^{n} \right\|_{\mathcal{E}}^{2} \right) + \left(\left\| {}^{d}\boldsymbol{\kappa}^{n+1} \right\|_{\mathcal{M}}^{2} - \left\| {}^{d}\boldsymbol{\kappa}^{n} \right\|_{\mathcal{M}}^{2} \right) + \left\| {}^{d}T^{n+1} \right\|_{\mathcal{T}}^{2} - \left\| {}^{d}T^{n} \right\|_{\mathcal{T}}^{2} \\
&= -\Delta t \underbrace{\int_{\Omega} {}^{d}\boldsymbol{v}_{J}^{n+\alpha} \cdot \mathbf{k}_{p,JK}{}^{-1} {}^{d}\boldsymbol{v}_{K}^{n+\alpha} d\Omega}_{\geq 0} - (2\alpha - 1) \left\| {}^{d}\boldsymbol{\varepsilon}^{n+1} - {}^{d}\boldsymbol{\varepsilon}^{n} \right\|_{\mathcal{E}}^{2} - (2\alpha - 1) \left\| {}^{d}\boldsymbol{\kappa}^{n+1} - {}^{d}\boldsymbol{\kappa}^{n} \right\|_{\mathcal{M}}^{2} \\
&\quad - (2\alpha - 1) \left\| {}^{d}T^{n+1} - {}^{d}T^{n} \right\|_{\mathcal{T}}^{2}. \qquad (49)
\end{aligned}
$$

Thus, the monolithic method yields unconditional stability, implying B-stability, when $0.5 \leq \alpha \leq 1.0$.

6. Stability and convergence of the sequential schemes

In this paper, we investigate stability and convergence of the two proposed sequential implicit methods. There are two ways to estimate numerical stability: spectral and energy methods. The spectral method can provide sharp stability and convergence estimates, while the energy method provides rigorous numerical stability estimates. For spectral analysis, we first investigate the error amplification factors under the backward Euler method, just as used in Kim et al. [17] and Kim et al. [18].

The error amplification factors are defined as the difference between the fully-implicit (monolithic method with $\alpha = 1.0$) and sequential methods. Since the fully-implicit method is unconditionally stable, as shown previously, we only examine by the spectral method the evolution of the errors between the fully coupled and sequential methods in order to investigate numerical stability. The error amplification factors can also estimate the rate of convergence for the sequential methods, when full iterations are taken.

6.1. Spectral analysis

We introduce a 1D thermoporomechanics problem. Let us assume no source terms, no capillarity, and homogeneous boundary conditions. Let $e_P^k = P^{n+1} - {P_s}^k$, $e_T^k = T^{n+1} - {T_s}^k$, and $e_{\varepsilon_v}^k = \varepsilon_v^{n+1} - \varepsilon_{v,s}^k$, where the subscript s, $(\cdot)_s$, denotes a sequential method. $(\cdot)^{n+1}$ is a solution from the fully-implicit method at t_{n+1}, so e^k is the error between the fully-implicit and sequential methods at t_{n+1}, when we perform a fixed number of iterations, where k is the iteration number. The undrained-adiabatic split solves the mechanical problem first, while freezing fluid mass content and heat at each grid block, so the error equation of mechanics in 1D is written as

$$
K_{ua}(e_{\varepsilon_{v,j-1}}^{k+1} - e_{\varepsilon_{v,j}}^{k+1}) - W_{ua}(e_{\varepsilon_{v,j-1}}^{k} - e_{\varepsilon_{v,j}}^{k}) - b(e_{P_{j-1}}^{k} - e_{P_j}^{k}) - 3\alpha_T K_{dr}(e_{T_{j-1}}^{k} - e_{T_j}^{k}) = 0,
$$

where

$$
K_{ua} = K_{dr} + W_{ua}, \quad W_{ua} = b^2 M + \frac{9\left(\alpha_T K_{dr} + \alpha_m b M\right)^2}{C_{ud}^*}, \qquad (50)
$$

where we label the elements with index j. For single fluid phase, b_J, M_{JK}, and $\alpha_{m,J}$ reduce to b, M, and α_m, respectively. The error equations for fluid and heat flow become, respectively,

$$\frac{h}{M}\frac{e_{P_j}^{k+1}}{\Delta t}+bh\frac{e_{\varepsilon_{v,j}}^{k+1}}{\Delta t}-3\alpha_m h\frac{e_{T_j}^{k+1}}{\Delta t}-\frac{k_p}{h}(e_{P_{j+1}}^{k+1}-2e_{P_j}^{k+1}+e_{P_{j-1}}^{k+1})$$
$$-\frac{h}{M}\frac{e_{P_j}^{n,n_{iter}}}{\Delta t}-bh\frac{e_{\varepsilon_{v,j}}^{n,n_{iter}}}{\Delta t}+3\alpha_m h\frac{e_{T_j}^{n,n_{iter}}}{\Delta t}=0, \tag{51}$$

$$C_T^* h\frac{e_{T_j}^{k+1}}{\Delta t}-3\alpha_m h\frac{e_{P_j}^{k+1}}{\Delta t}+3\alpha_T K_{dr} h\frac{e_{\varepsilon_{v,j}}^{k+1}}{\Delta t}-\frac{k_T}{\mu}\frac{1}{h}(e_{T_{j+1}}^{k+1}-2e_{T_j}^{k+1}+e_{T_{j-1}}^{k+1})-\frac{v_T}{h}(e_{T_j}^{k+1}-e_{T_{j-1}}^{k+1})$$
$$+3\alpha_m h\frac{e_{P_j}^{n,n_{iter}}}{\Delta t}-3\alpha_T K_{dr} h\frac{e_{\varepsilon_{v,j}}^{n,n_{iter}}}{\Delta t}-C_T^* h\frac{e_{T_j}^{n,n_{iter}}}{\Delta t}=0, \tag{52}$$

where h is the grid spacing. We use the upstream weighting for the heat convection term, so v_T is positive. n_{iter} is the number of iterations. We neglect the terms associated with $(\cdot)^{n,n_{iter}}$ because we only investigate error amplification during iteration at the current time step.

Let us introduce errors of the form $e_{\varepsilon_{v,j}}^k=\gamma_e^k e^{i(j)\theta}e_{\hat{\varepsilon_v}}$, $e_{P_j}^k=\gamma_e^k e^{i(j)\theta}e_{\hat{P}}$, and $e_{T_j}^k=\gamma_e^k e^{i(j)\theta}e_{\hat{T}}$ to Equations 50, 51, and 52, where γ_e, i, and θ ($-\pi\le\theta\le\pi$) are the error amplification factor, imaginary unit, and phase, respectively. Then, we obtain

$$\underbrace{\begin{bmatrix}(K_{dr}+W_{ua})\gamma_e-W_{ua} & -b & -3\alpha_T K_{dr}\\ b\gamma_e & \left(\frac{1}{M}+2(1-\cos\theta)\frac{k_p\Delta t}{h^2}\right)\gamma_e & -3\alpha_m\gamma_e\\ 3\alpha_T K_{dr}\gamma_e & -3\alpha_m\gamma_e & \left(C_d^*+2(1-\cos\theta)\frac{k_T\Delta t}{h^2}\right.\\ & & \left.+(1-\cos\theta+i\sin\theta)\frac{v_T\Delta t}{h}\right)\gamma_e\end{bmatrix}}_{\mathbf{E}_{ua}}\begin{bmatrix}e_{\hat{\varepsilon_v}}\\ e_{\hat{P}}\\ e_{\hat{T}}\end{bmatrix}=\begin{bmatrix}0\\0\\0\end{bmatrix}. \tag{53}$$

From $\det(\mathbf{E}_{ua})=0$, we have the error amplification factors as

$$\begin{aligned}\gamma_{e,ua} &= 0,\ \frac{a_0 W_{ua}-a_1}{a_0\left(K_{dr}+W_{ua}\right)}, \\ a_0 &= \left(\frac{1}{M}+2(1-\cos\theta)\frac{k_p\Delta t}{h^2}\right)\left(C_d^*+2(1-\cos\theta)\frac{k_T\Delta t}{h^2}+(1-\cos\theta+i\sin\theta)\frac{v_T\Delta t}{h}\right)-9\alpha_m^2, \\ a_1 &= b^2\left(C_d^*+2(1-\cos\theta)\frac{k_T\Delta t}{h^2}+(1-\cos\theta+i\sin\theta)\frac{v_T\Delta t}{h}\right) \\ &+ 18\alpha_T K_{dr}\alpha_m+9\alpha_T^2 K_{dr}^2\left(\frac{1}{M}+2(1-\cos\theta)\frac{k_p\Delta t}{h^2}\right).\end{aligned} \tag{54}$$

The necessary condition for stability is $\max|\gamma_e|\le 1$ for all θ. We numerically calculate the error amplification factors, taking wide ranges of flow and geomechanics properties in Equation 54 (Figure 2). We find from the figure that the amplification factors are between 0 and 1, being positive. This implies that the undrained-adiabatic split is unconditionally stable and monotonic.

From Figure 2, we also find that the amplification factors are maximum at $\theta=-\pi,\pi$. For isothermal poroelasticity, $\max|\gamma_e|$ was found at $\theta=-\pi,\pi$, too [17, 18]. At $\theta=-\pi,\pi$, we have $|a_0\left(K_{dr}+W_{ua}\right)|\ge|a_0 W_{ua}-a_1|$ from Equation 54, yielding $\max|\gamma_e|\le 1$. Then, we confirm that the undrained-adiabatic split is unconditionally stable.

In the similar fashion, the extended fixed-stress split yields

$$\underbrace{\begin{bmatrix} K_{dr}\gamma_e & -b\gamma_e & -3\alpha_T K_{dr}\gamma_e \\ b & \left(\frac{1}{M}+2(1-\cos\theta)\frac{k_p\Delta t}{h^2}+\frac{b^2}{K_{dr}}\right)\gamma_e-\frac{b^2}{K_{dr}} & -3(\alpha_m-b\alpha_T)\gamma_e-3b\alpha_T \\ 3\alpha_T K_{dr} & -3(\alpha_m-b\alpha_T)\gamma_e-3b\alpha_T & \left(C_d^*+2(1-\cos\theta)\frac{k_T\Delta t}{h^2}\right. \\ & & \left.+(1-\cos\theta+i\sin\theta)\frac{v_T\Delta t}{h}\right. \\ & & \left.+9\alpha_T^2 K_{dr}\right)\gamma_e-9\alpha_T^2 K_{dr} \end{bmatrix}}_{\mathbf{E}_{ef}} \begin{bmatrix} \hat{e_{\varepsilon_v}} \\ \hat{e_P} \\ \hat{e_T} \end{bmatrix} = \begin{bmatrix} 0 \\ 0 \\ 0 \end{bmatrix}. \tag{55}$$

From $\det(\mathbf{E}_{ef})=0$, we obtain the error amplification factors for the extended fixed-stress split as

$$\gamma_{e,ss} \;=\; 0 \;\; (\text{multiple}), \tag{56}$$

which yields unconditional stability.

Remark 3. Unlike the undrained-adiabatic split, the extended fixed-stress split has the zero error amplification factor, which means that it can match the fully coupled method by two iterations when the local K_{dr} can be exactly estimated, as shown in the isothermal case [18]. On the other hand, for the undrained-adiabatic split, when the fluid and solid grains are incompressible or the undrained heat capacity approaches zero (i.e., $M=\infty$ or $C_*^{ud}\approx 0$), we have $W_{ua}=\infty$. In this limit, we have $\max|\gamma_{e,\,ua}|\approx 1$, which causes non-convergence for the undrained-adiabatic split even though it is stable.

6.2. Energy method

6.2.1. Dissipative character of the undrained-adiabatic and extended fixed-stress splits

We first investigate the dissipative character of the undrained-adiabatic split. We take the same approach used to show the dissipative nature of thermoporomechanics and numerical stability of the monolithic method. At the mechanics step, we have

$$\mathrm{Div}\,{}^d\boldsymbol{\sigma}=\mathbf{0},\;\; {}^d\dot{m}_J=0,\;\; {}^d\dot{\bar{S}}=0, \tag{57}$$

which yields

$$\begin{aligned} \frac{d\left\|{}^d\chi\right\|_{\mathcal{N}}^2}{dt} &= \frac{\partial\left\|{}^d\chi\right\|_{\mathcal{N}}^2}{\partial^d\boldsymbol{\varepsilon}} : {}^d\dot{\boldsymbol{\varepsilon}} + \frac{\partial\left\|{}^d\chi\right\|_{\mathcal{N}}^2}{\partial^d m_J}\,{}^d\dot{m}_J + \frac{\partial\left\|{}^d\chi\right\|_{\mathcal{N}}^2}{\partial^d T}\,{}^d\dot{T} \\ &= \int_\Omega \left({}^d\boldsymbol{\sigma} : {}^d\dot{\boldsymbol{\varepsilon}} + \left(\frac{{}^dp}{\rho}\right)_J \underbrace{{}^d\dot{m}_J}_{=0} + T(\underbrace{{}^d\dot{\bar{S}}}_{=0} - \bar{s}_J \underbrace{{}^d\dot{m}_J}_{=0}) \right) d\Omega \\ &= \int_\Omega {}^d\boldsymbol{\sigma} : {}^d\dot{\boldsymbol{\varepsilon}}\, d\Omega = 0, \end{aligned} \tag{58}$$

which shows the dissipative character relative to the norms, $\|\cdot\|_{\mathcal{N}}$.

After the mechanics step, we take the fluid and heat flow step, having

$$ {}^{d}\dot{m}_J = -\operatorname{Div}{}^{d}\boldsymbol{w}_J, \quad {}^{d}T\left({}^{d}\dot{\bar{S}} - \bar{s}_J{}^{d}\dot{m}_J\right) = -\operatorname{Div}({}^{d}\boldsymbol{f}_T), \quad {}^{d}\boldsymbol{\varepsilon} = \mathbf{0}. \tag{59} $$

Considering no perturbation on $\dot{\boldsymbol{\varepsilon}}$ in Equation 59, we have the dissipative character relative to the norm, $\|\cdot\|_{\mathcal{N}}$ as

$$ \begin{aligned}
\frac{d\left\|{}^{d}\chi\right\|_{\mathcal{N}}^{2}}{dt} &= \frac{\partial\left\|{}^{d}\chi\right\|_{\mathcal{N}}^{2}}{\partial{}^{d}m_J}{}^{d}\dot{m}_J + \frac{\partial\left\|{}^{d}\chi\right\|_{\mathcal{N}}^{2}}{\partial{}^{d}T}{}^{d}\dot{T} \\
&= \int_{\Omega}\Big(\left(\frac{{}^{d}m}{\rho}\right)_J M_{JK}\left(\frac{{}^{d}\dot{m}}{\rho}\right)_K + C^{*}_{ud}{}^{d}T{}^{d}\dot{T}\Big)d\Omega \\
&= \int_{\Omega}\Big(\left({}^{d}p_K - 3\alpha_{m,J}{}^{d}TM_{JK}\right)\left(\frac{{}^{d}\dot{m}}{\rho}\right)_K + (C^{*}_{d} - 9\alpha_{m,J}M_{JK}\alpha_{m,K})^{d}T{}^{d}\dot{T}\Big)d\Omega \\
&= \int_{\Omega}\Big(\left(\frac{{}^{d}p}{\rho}\right)_J{}^{d}\dot{m}_J - 3\alpha_{m,J}{}^{d}T\left({}^{d}\dot{p}_J - M_{JK}3\alpha_{m,K}{}^{d}\dot{T}\right) + (C^{*}_{d} - 9\alpha_{m,J}M_{JK}\alpha_{m,K})^{d}T{}^{d}\dot{T}\Big)d\Omega \\
&= \int_{\Omega}\Big(\left(\frac{{}^{d}p}{\rho}\right)_J{}^{d}\dot{m}_J - 3\alpha_{m,J}{}^{d}T{}^{d}\dot{p}_J + {}^{d}T\left({}^{d}\dot{\bar{S}} - \bar{s}_J{}^{d}\dot{m}_J + 3\alpha_{m,J}{}^{d}\dot{p}_J\right)\Big)d\Omega \\
&= \int_{\Omega}\left(\frac{{}^{d}p}{\rho}\right)_J{}^{d}\dot{m}_J + {}^{d}T\left({}^{d}\dot{\bar{S}} - \bar{s}_J{}^{d}\dot{m}_J\right)d\Omega \\
&= \int_{\Omega}\left(-{}^{d}p_J\operatorname{Div}{}^{d}\boldsymbol{v}_J - \operatorname{Div}{}^{d}\boldsymbol{f}_T\right)d\Omega \\
&= -\int_{\Omega}\underbrace{{}^{d}\boldsymbol{v}_J\cdot\mathbf{k}^{-1}_{p,JK}{}^{d}\boldsymbol{v}_K}_{\geq 0}d\Omega - \underbrace{\int_{\Gamma}{}^{d}\boldsymbol{f}_T\cdot n d\Gamma}_{=0} \leq 0.
\end{aligned} \tag{60} $$

Thus, the undrained-adiabatic split shows the dissipative character relative to the norm, $\|\cdot\|_{\mathcal{N}}$, being contractive.

Next, we investigate the dissipative character of the extended fixed-stress split. At the flow step, we have

$$ {}^{d}\dot{m}_J + \operatorname{Div}{}^{d}\boldsymbol{w}_J = 0, \quad {}^{d}T\left({}^{d}\dot{S} - s_J{}^{d}\dot{m}_J\right) = -\operatorname{Div}({}^{d}\boldsymbol{f}_T), \quad \delta{}^{d}\dot{\boldsymbol{\sigma}} = 0, \tag{61} $$

where the initial conditions of the flow problem, $\mathcal{A}^{fl}_{ss}$, are

$$ \operatorname{Div}\dot{\sigma}_{t=0} = 0\,, \quad \operatorname{Div}\sigma_{t=0} = 0. \tag{62} $$

Consider $\delta{}^{d}\dot{\boldsymbol{\sigma}} = 0$, which yields ${}^{d}\dot{\boldsymbol{\sigma}}(t) - {}^{d}\dot{\boldsymbol{\sigma}}_{t=0} = \mathbf{0}$. Combining this result with Equation 62_1, we have ,

$$ \operatorname{Div}{}^{d}\dot{\boldsymbol{\sigma}}(t) = \operatorname{Div}{}^{d}\dot{\boldsymbol{\sigma}}_{t=0} = 0. \tag{63} $$

Note that the divergence operator, Div, is not a function of time under infinitesimal transformation, which provides $\operatorname{Div}{}^{d}\dot{\boldsymbol{\sigma}}(t) = \partial_t\operatorname{Div}{}^{d}\boldsymbol{\sigma}(t)$. Hence, from Equations 62_2 and 63, we obtain

$$ \operatorname{Div}{}^{d}\boldsymbol{\sigma}(t) = \operatorname{Div}{}^{d}\boldsymbol{\sigma}(t)_{t=0} = 0. \tag{64} $$

Then, Equations 61 and 64 satisfy Equation 33, from which the extended fixed-stress split is dissipative relative to the norm, $\|\cdot\|_{\mathcal{N}}$. After the flow step, we take the mechanics step, having

$$\mathrm{Div}\,{}^{d}\boldsymbol{\sigma} = \mathbf{0},\ {}^{d}p_J = \mathbf{0},\ {}^{d}T = \mathbf{0}, \Rightarrow \mathrm{Div}\,{}^{d}\boldsymbol{\sigma}' = \mathbf{0}, \tag{65}$$

which yields dissipative character as

$$\frac{d\left\|{}^{d}\chi\right\|_{\mathcal{N}}^{2}}{dt} = \frac{\partial\left\|{}^{d}\chi\right\|_{\mathcal{N}}^{2}}{\partial\boldsymbol{\varepsilon}} : \dot{\boldsymbol{\varepsilon}} = \underbrace{\int_{\Omega} {}^{d}\boldsymbol{\sigma}' : {}^{d}\boldsymbol{\varepsilon} d\Omega}_{=0} \leq 0.$$

Thus, the extended fixed-stress split shows the dissipative character relative to the norm, $\|\cdot\|_{\mathcal{N}}$, being contractive, during both flow and mechanics steps.

6.2.2. Numerical stability of the undrained-adiabatic and extended fixed-stress splits

Since the undrained-adiabatic and extended fixed-stress splits are dissipative, we study the two sequential schemes on algorithmic stability of them. We first perform stability analysis of the undrained-adiabatic split. At the mechanics step, the undrained-adiabatic split satisfies,

$$\mathrm{Div}\,{}^{d}\boldsymbol{\sigma}^{n+\alpha} = \mathbf{0},\ \Delta^{d}m_J^n = 0,\ \Delta^{d}\bar{S}^n = 0, \tag{66}$$

where the second and third equations (undrained and adiabatic conditions, respectively) lead to

$${}^{d}\boldsymbol{v}_J^{n+\alpha} = 0,\ {}^{d}\boldsymbol{f}_T^{n+\alpha} = 0. \tag{67}$$

Referring to Equations 41– 48 and using Equations 66 and 67, we have

$$\begin{aligned}
&\left\|{}^{d}\chi^{n+1}\right\|_{\mathcal{N}}^{2} - \left\|{}^{d}\chi^{n}\right\|_{\mathcal{N}}^{2} \\
&= \left(\left\|{}^{d}\boldsymbol{\varepsilon}^{n+1}\right\|_{\mathcal{E}}^{2} - \left\|{}^{d}\boldsymbol{\varepsilon}^{n}\right\|_{\mathcal{E}}^{2}\right) + \left(\left\|{}^{d}\boldsymbol{\kappa}^{n+1}\right\|_{\mathcal{M}}^{2} - \left\|{}^{d}\boldsymbol{\kappa}^{n}\right\|_{\mathcal{M}}^{2}\right) + \left(\left\|{}^{d}T^{n+1}\right\|_{\mathcal{T}}^{2} - \left\|{}^{d}T^{n}\right\|_{\mathcal{T}}^{2}\right) \\
&= 0 + \int_{\Omega} \Delta^{d}\varepsilon_v^n b_J {}^{d}p_J^{n+\alpha} d\Omega + \int_{\Omega} \Delta^{d}\varepsilon_v^n 3\alpha_T K_{dr} {}^{d}T^{n+\alpha} d\Omega - (2\alpha-1)\left\|{}^{d}\boldsymbol{\varepsilon}^{n+1} - {}^{d}\boldsymbol{\varepsilon}^{n}\right\|_{\mathcal{E}}^{2} \\
&\quad + \int_{\Omega} {}^{d}p_K^{n+\alpha} \underbrace{\left(\frac{\Delta^{d}m^n}{\rho}\right)_K}_{=0} d\Omega - \int_{\Omega} \Delta^{d}\varepsilon_v^n b_J {}^{d}p_J^{n+\alpha} d\Omega - \int_{\Omega} 3{}^{d}T^{n+\alpha}\alpha_{m,J} \underbrace{M_{JK}\left(\left(\frac{{}^{d}\Delta m^n}{\rho}\right)_K - b_K \Delta^{d}\varepsilon_v^n\right)}_{\Delta^{d}p_J^n - 3\alpha_{m,K}M_{JK}\Delta^{d}T^n} d\Omega \\
&\quad - (2\alpha-1)\left\|{}^{d}\boldsymbol{\kappa}^{n+1} - {}^{d}\boldsymbol{\kappa}^{n}\right\|_{\mathcal{M}}^{2} \\
&\quad + \int_{\Omega} {}^{d}T^{n+\alpha}\left(\underbrace{\Delta^{d}\bar{S}^n}_{=0} - \bar{s}_J^{n+\alpha}\underbrace{\Delta^{d}m_J{}^n}_{=0} - 3\alpha_T K_{dr}\Delta^{d}\varepsilon_v^n + 3\alpha_{m,J}\Delta^{d}p_J^n\right) - 9\alpha_{m,J}M_{JK}\alpha_{m,K}{}^{d}T^{n+\alpha}\Delta^{d}T^n d\Omega \\
&\quad - (2\alpha-1)\left\|{}^{d}T^{n+1} - {}^{d}T^{n}\right\|_{\mathcal{T}}^{2} \\
&= -(2\alpha-1)\left\|{}^{d}\boldsymbol{\varepsilon}^{n+1} - {}^{d}\boldsymbol{\varepsilon}^{n}\right\|_{\mathcal{E}}^{2} - (2\alpha-1)\left\|{}^{d}\boldsymbol{\kappa}^{n+1} - {}^{d}\boldsymbol{\kappa}^{n}\right\|_{\mathcal{M}}^{2} - (2\alpha-1)\left\|{}^{d}T^{n+1} - {}^{d}T^{n}\right\|_{\mathcal{T}}^{2},
\end{aligned} \tag{68}$$

from which we have unconditional stability when $0.5 \leq \alpha \leq 1$. After solution of geomechanics, we have at the flow step

$$\Delta^d m_J{}^n = -\Delta t \,\mathrm{Div}\,{}^d\boldsymbol{w}_J^{n+\alpha}, \quad T^{n+\alpha}\left(\Delta^d \bar{S}^n - \bar{s}_J \Delta^d m_J{}^n\right) = -\Delta t \,\mathrm{Div}\,{}^d\boldsymbol{f}_T^{n+\alpha}, \quad {}^d\boldsymbol{\varepsilon}^n = {}^d\boldsymbol{\varepsilon}^{n+1} = 0. \tag{69}$$

Referring to Equations 42– 48, Equation 69 provides

$$\begin{aligned}
&\left\|{}^d\chi^{n+1}\right\|_{\mathcal{N}}^2 - \left\|{}^d\chi^n\right\|_{\mathcal{N}}^2 \\
&= \; 0 + \left(\left\|{}^d\boldsymbol{\kappa}^{n+1}\right\|_{\mathcal{M}}^2 - \left\|{}^d\boldsymbol{\kappa}^n\right\|_{\mathcal{M}}^2\right) + \left(\left\|{}^dT^{n+1}\right\|_{\mathcal{T}}^2 - \left\|{}^dT^n\right\|_{\mathcal{T}}^2\right) \\
&= -\Delta t \underbrace{\int_\Omega {}^d\boldsymbol{v}_J^{n+\alpha}\cdot \mathbf{k}_{p,JK}{}^{-1}\,{}^d\boldsymbol{v}^{n+\alpha}{}_K d\Omega}_{\geq 0} - \int_\Omega \underbrace{\Delta^d\varepsilon_v^n}_{=0} b_J\,{}^d p_J^{n+\alpha} d\Omega \\
&\quad - \int_\Omega 3\,{}^dT^{n+\alpha}\alpha_{m,J} M_{JK}\Delta^d\boldsymbol{\kappa}_K^n d\Omega - (2\alpha-1)\left\|{}^d\boldsymbol{\kappa}^{n+1} - {}^d\boldsymbol{\kappa}^n\right\|_{\mathcal{M}}^2 \\
&\quad - \Delta t \underbrace{\int_\Gamma {}^d\boldsymbol{f}_T^{n+\alpha}\cdot n d\Gamma}_{=0} - \int_\Omega \underbrace{\Delta^d\varepsilon_v^n}_{=0} 3\alpha_T K_{dr}\,{}^dT^{n+\alpha} d\Omega + \int_\Omega 3\,{}^dT^{n+\alpha}\alpha_{m,J} M_{JK}\Delta^d\kappa_K^n d\Omega \\
&\quad - (2\alpha-1)\left\|{}^dT^{n+1} - {}^dT^n\right\|_{\mathcal{T}}^2 \\
&= \; -\Delta t \int_\Omega {}^d\boldsymbol{v}_J^{n+\alpha}\cdot \mathbf{k}_{p,JK}{}^{-1}\,{}^d\boldsymbol{v}_K^{n+\alpha} d\Omega - (2\alpha-1)\left\|{}^d\boldsymbol{\kappa}^{n+1} - {}^d\boldsymbol{\kappa}^n\right\|_{\mathcal{M}}^2 - (2\alpha-1)\left\|{}^dT^{n+1} - {}^dT^n\right\|_{\mathcal{T}}^2
\end{aligned} \tag{70}$$

from which we have unconditional stability when $0.5 \leq \alpha \leq 1$. Thus, from Equations 68 and 70, the undrained-adiabatic split is unconditionally stable when $0.5 \leq \alpha \leq 1$.

For the extended fixed-stress split, the flow step is solved first, having

$$\Delta^d m_J{}^n = -\Delta t \,\mathrm{Div}\,{}^d\boldsymbol{w}_J^{n+\alpha}, \quad T^{n+\alpha}\left(\Delta^d \bar{S}^n - \bar{s}_J\,{}^d\Delta m_J{}^n\right) = -\Delta t \,\mathrm{Div}\,{}^d\boldsymbol{f}_T^{n+\alpha}, \quad \Delta^d\boldsymbol{\sigma}^n = \Delta^d\boldsymbol{\sigma}^{n-1}, \tag{71}$$

satisfying

$$\mathrm{Div}\,\Delta^d\boldsymbol{\sigma}^0 = 0\,, \quad \mathrm{Div}\,{}^d\boldsymbol{\sigma}^0 = 0. \tag{72}$$

From Equation 71_3, we have

$$\Delta^d\boldsymbol{\sigma}^n = \Delta^d\boldsymbol{\sigma}^{n-1} = \cdots = \Delta^d\boldsymbol{\sigma}^0 \tag{73}$$

We then obtain from Equations 72 and 73

$$\mathrm{Div}\,{}^d\boldsymbol{\sigma}^{n+1} = \mathrm{Div}\,{}^d\boldsymbol{\sigma}^n = \cdots = 0, \Rightarrow \mathrm{Div}\,{}^d\boldsymbol{\sigma}^{n+\alpha} = 0. \tag{74}$$

Since the extended fixed-stress split satisfies Equations 35– 37, it provides Equation 49, which implies unconditional stability when $0.5 \leq \alpha \leq 1$.

After solution of flow, we have at the mechanics step

$$\mathrm{Div}\,{}^{d}\boldsymbol{\sigma}^{n+\alpha} = \mathbf{0}, \quad {}^{d}p_J = 0, \quad {}^{d}T = 0, \Rightarrow \mathrm{Div}\,{}^{d}\boldsymbol{\sigma}'^{n+\alpha} = \mathbf{0}, \tag{75}$$

which satisfies

$$\int_{\Omega} {}^{d}\boldsymbol{\varepsilon}^{n+\alpha} : \mathbf{C}_{dr}\Delta^{d}\boldsymbol{\varepsilon}^{n} d\Omega = 0. \tag{76}$$

Also, ${}^{d}p_J^{n+\alpha} = 0$ and ${}^{d}T^{n+\alpha} = 0$ yield respectively

$$\int_{\Omega} {}^{d}p_J^{n+\alpha} \left(\frac{\Delta^{d}m^{n}}{\rho}\right)_J d\Omega = 0, \; \int_{\Omega} {}^{d}T^{n+\alpha} C_{ud}^{*} \Delta^{d}T^{n} d\Omega = 0. \tag{77}$$

Then, we obtain

$$\begin{aligned} & \left\|{}^{d}\chi^{n+1}\right\|_{\mathcal{N}}^{2} - \left\|{}^{d}\chi^{n}\right\|_{\mathcal{N}}^{2} \\ = \; & \left(\left\|{}^{d}\boldsymbol{\varepsilon}^{n+1}\right\|_{\mathcal{E}}^{2} - \left\|{}^{d}\boldsymbol{\varepsilon}^{n}\right\|_{\mathcal{E}}^{2}\right) + 0 + 0 \\ = \; & 0 - (2\alpha - 1)\left\|{}^{d}\boldsymbol{\varepsilon}^{n+1} - {}^{d}\boldsymbol{\varepsilon}^{n}\right\|_{\mathcal{E}}^{2}, \end{aligned}$$

from which we have unconditional stability when $0.5 \leq \alpha \leq 1$. As a result, for both steps, the extended fixed-stress split is unconditionally stable, when $0.5 \leq \alpha \leq 1$.

Remark 4. The two sequential methods may take different time integration methods at the steps of fluid-heat flow and geomechanics, having different α's. For example, we can take the backward Euler method, $\alpha_{mech} = 1.0$ for geomechanics, while taking the midpoint rule, $\alpha_{fl} = 0.5$, for the flow. Still, this mixed time integration provides unconditional stability.

7. Numerical results

We take three one-dimensional (1D) coupled flow-geomechanics test cases. The first two cases (Cases 1 and 2) are used for poro-mechanics and thermo-mechanics problems, respectively, in order to verify the simulation code. For the third case (Case 3), we then employ a scenario of all-way coupled thermo-poro-mechanics and investigate numerical stability. No gravity is considered in the test cases.

7.1. Case 1: isothermal poromechanics

We first use an isothermal one-dimensional (1D) consolidation problem (Terzaghi's problem), as shown in the left of Figure 2. The 1D domain is divided into 20 uniformly-sized gridblocks in the z direction with $\Delta x = 1\ m$, $\Delta y = 1\ m$, and $\Delta z = 2\ m$. For flow, the fluid compressibility is $c_f = 3.0 \times 10^{-8}\ Pa^{-1}$. The density and viscosity are $\rho_f = 1000$ kg m^{-1} and $\mu_f = 1.0$ cp. Initial fluid pressure and porosity are also $P_i = 2.125\ MPa$ and $\phi_0 = 0.3$. We have drainage boundaries at top and bottom, having constant pressure of $P_i = 2.125\ MPa$. Permeability is $k_p = 49.35 \times 10^{-15}\ m^2$, 50 md, being constant during simulation. For mechanics, linear elasticity is considered. Both

drained and constrained bulk moduli are $K_c = K_{dr} = 100\ MPa$, respectively. We have a no-displacement boundary at the bottom, while the overburden, $\bar{\sigma} = 2 \times 2.125 MPa$, is applied to the top boundary. We take the initial total stress of $-2.125\ MPa$, resulting in no strain changes at $t = 0$. Biot's coefficient is $b = 1.0$, which yields $K_s = \infty$. The analytical solution for this case is given as

$$\frac{p_f(z,t)}{p_0} = \frac{4}{\pi}\sum_{j=1}^{\infty}\frac{(-1)^{j-1}}{2j-1}cos\left[(2j-1)\frac{\pi}{2}\frac{L_z - z}{L_z}\right]exp\left[-(2j-1)^2\frac{\pi^2}{4}\frac{c_v t}{L_z^2}\right], \tag{78}$$
$$p_0 = -\frac{1/K_{dr}}{1/K_{dr} + \phi c_f}\Delta\sigma_z,\ \ c_v = \frac{k_p}{(1/K_{dr} + \phi c_f)\mu_f},$$

where $b = 1.0$ and c_v is the consolidation coefficient. p_0 is the instantaneous pressure build-up at the initial time due to the instantaneous external mechanical loading at the top.

From the left of Figure 4, numerical solutions of the fully-implicit, undrained-adiabatic, and extended fixed-stress methods match the analytical solution, being monotonic. This result verifies the simulator for isothermal poromechanics.

7.2. Case 2: thermoelasticity

We consider a (1D) thermo-mechanical problem, as shown in the center of Figure 2, having the same discretized domain of Case 1. Just like Case 1, we generate thermal flow induced by deformation, taking strong coupling between thermal flow and mechanics synthetically. Then, similar to Equation 78, the analytical solution of this case becomes

$$\frac{T(z,t)}{T_0} = \frac{4}{\pi}\sum_{j=1}^{\infty}\frac{(-1)^{j-1}}{2j-1}cos\left[(2j-1)\frac{\pi}{2}\frac{L_z - z}{L_z}\right]exp\left[-(2j-1)^2\frac{\pi^2}{4}\frac{d_T t}{L_z^2}\right], \tag{79}$$
$$T_0 = -\frac{1}{C_d^* + 3\alpha_T K_{dr}}\Delta\sigma_z,\ \ d_T = \frac{k_T}{C_d^* + 9\alpha_T^2 K_{dr}},$$

where T_0 is the instantaneous temperature build-up at the initial time due to the instantaneous external mechanical loading at the top. Specifically, for Case 2, we have a specific heat capacity of $1.90 kJ\ kg^{-1}\ {}^oC^{-1}$, high heat conductivity of $k_T = 85\ Wm^{-1}\ {}^oC^{-1}$, and thermal dilation (coupling) coefficient of $\alpha_T = 10^{-2}\ {}^oC^{-1}$. The initial temperature is $T_i = 25^oC (= 298.15\ K)$. We have constant temperature of $T_i = 25^oC (= 298.15\ K)$ at top and bottom. For mechanics, we take $K_{dr} = K_c = 10\ MPa$ and the initial total stress of $0\ MPa$. The no-displacement boundary is applied at the bottom, while the overburden of $\bar{\sigma} = 2.125\ MPa$ is at the top.

We find from the right of Figure 4 that the numerical results of the fully-implicit, undrained-adiabatic, and extended fixed-stress methods match the analytical solution. These results also verify the simulator for thermomechanics.

7.3. Case 3: all-way coupled thermoporomechanics

We consider a 1D thermoporomechanics problem (the right of Figure 2), taking the same discretized domain of Case 1. For fluid flow and mechanics, we have the conditions same as Case 1, except that no-flow of fluid is applied to the bottom. For thermal flow, we have specific heat capacities of $0.92\ kJ\ kg^{-1}{}^oC^{-1}$ and $4.18\ kJ\ kg^{-1}{}^oC^{-1}$ for the porous medium and fluid, respectively. The bulk heat conductivity is $k_T = 1.7\ Wm^{-1}{}^oC^{-1}$. We specify constant

temperatures of 25^oC and 75^oC at the top and bottom, respectively. We take $\alpha_m = 0$ and $\alpha_\phi = 0$. We inject fluid with a total mass rate of $Q_i = 100\ kg/day$, while no external heat injection is considered. Then, we investigate numerical stability of the undrained-adiabatic and extended fixed-stress methods for various thermal dilation coefficients.

Figures 5 and 6 show evolutions of pressure and temperature from the fully-implicit, undrained-adiabatic, and extended fixed-stress methods. In Figure 5, the pressure at the monitoring point decreases, as the coupling coefficient between thermal flow and mechanics (α_T) increases, because high α_T induces more thermal expansion as temperature increases. The thermal expansion of the porous medium increases the expansion of pore-volume, which results in the pressure drop due to fluid compressibility. Figure 6 shows the temperature changes for various α_T, and we find the lowest temperature, when $\alpha_T = 10^{-3o}C^{-1}$. Thermal dilation affects heat flow, in turn, as a sink term, resulting in retardation of thermal flow.

We find from Figures 5 and 6 that the two sequential methods provide stable and reliable solutions, comparable to the fully-implicit method. When fluid becomes incompressible, the undrained-adiabatic method is less accurate, whereas the extended fixed-stress method still shows good accuracy. The left of Figure 7 shows that the error amplification factor of the undrained-adiabatic method approaches one, which implies almost non-convergence. On the other hand, the error amplification factor of the extended fixed-stress method is not affected by fluid compressibility. From the center and right of Figure 7, we identify non-convergence of the undrained-adiabatic method for nearly incompressible fluid. Figure 8 also shows that the extended fixed-stress method still shows good accuracy whereas the undrained-adiabatic method exhibits inaccuracy.

In multiple dimensions, it might be difficult to exactly estimate the drained bulk modulus used in the flow problem. Let us define the deviation factor of $\eta = K_{dr}^{exact}/K_{dr}^{est}$, defined as the ratio of the exact local drained bulk modulus to the estimated local drained bulk modulus. As discussed in Kim et al. [18] and Kim et al. [20] for isothermal poromechanics, the 3D drained bulk modulus is a safe choice for stability and convergence for all 1D, 2D, 3D problems, yielding $1 < \eta < 3$. From Figure 9, the extended fixed-stress method is still accurate, matching the reference solutions, when $\eta = 3$. When the time step size is refined, we obtain more accurate results of pressure and temperature, which implies numerical convergence of the extended fixed-stress method.

From the stability analysis, we can take the mixed time stepping algorithms for flow and geomechanics in the two sequential methods (i.e., different α's). Figure 10 shows the numerical results when we take $\alpha = 0.6$ for heat-fluid flow and $\alpha = 1.0$ for mechanics, respectively, in the two sequential methods. Comparing the results of the two sequential methods with the fully-implicit method, we find that the mixed time stepping in both sequential methods still yields stable solutions, supporting the stability analysis.

8. Conclusions

We proposed two unconditionally stable sequential methods for all-way coupled thermoporomechanics problems: the undrained-adiabatic split and the extended fixed-stress split. We showed that the two sequential methods are unconditionally stable, when taking $0.5 \leq \alpha \leq 1.0$ for sub-problems of flow and mechanics. From the numerical tests, both undrained-adiabatic and extended fixed-stress splits were stable. Thus, the two sequential methods can also

be used as reliable preconditioners for the fully-implicit method. When stable individual simulators of non-isothermal flow and geomechanics are available, the undrained-adiabatic and extended fixed-stress splits can straightforwardly be applied in solving all-way coupled thermo-poro-mechanical problems.

9. Acknowledgements

This study was supported by the U.S. Department of Energy (Award No. DE-FE0028973), Methane Hydrate Program.

References

[1] T. Xu, E. Sonnenthal, N. Spycher, K. Pruess, TOUGHREACT: A simulation program for non-isothermal multiphase reactive geochemical transport in variably saturated geologic media: Applications to geothermal injectivity and CO2 geological sequestration, Computers and Geosciences 32 (2006) 145–156.

[2] J. Taron, D. Elsworth, Coupled Mechanical and Chemical Processes in Engineered Geothermal Reservoirs with Dynamic Permeability, International Journal of Rock Mechanics and Mining Sciences 47 (2010) 1339 – 1348.

[3] J. Kim, E. Sonnenthal, J. Rutqvist, Formulation and sequential numerical algorithms of coupled fluid/heat flow and geomechanics for multiple porosity materials., International Journal for Numerical Methods in Engineering 92 (2012) 425–456.

[4] J. Rutqvist, G. J. Moridis, Numerical Studies on the Geomechanical Stability of Hydrate-Bearing Sediments, SPE Journal 14 (2) (2009) 267–282.

[5] G. J. Moridis, J. Kim, M. T. Reagan, S. Kim, Feasibility of gas production from a gas hydrate accumulation at the UBGH2-6 site of the Ulleung basin in the Korean East Sea, Journal of Petroleum Science and Engineering 108 (2013) 180 – 210.

[6] J. Rutqvist, D. Barr, J. T. Birkholzer, K. Fujisaki, O. Kolditz, Q.-S. . Liu, T. Fujita, W. Wang, C.-Y. Zhang, A comparative simulation study of coupled THM processes and their effect on fractured rock permeability around nuclear waste repositories, Environmental Geology 57 (2009) 1347–1360.

[7] J. Rutqvist, B. Freifeld, K.-B. Min, D. Elsworth, Y. Tsang, Analysis of thermally induced changes in fractured rock permeability during eight years of heating and cooling at the Yucca Mountain Drift Scale Test, International Journal of Rock Mechanics and Mining Sciences 45 (2008) 1375–1389.

[8] O. Coussy, Poromechanics of Freezing Materials, Journal of the Mechanics and Physics of Solids (2005) 1689–1718.

[9] F. Armero, J. C. Simo, A new unconditionally stable fractional step method for non-linear coupled thermomechanical problems, International Journal for Numerical Methods in Engineering 35 (1992) 737–766.

[10] A. Settari, D. A. Walters, Advances in coupled geomechanical and reservoir modeling with applications to reservoir compaction, SPE Journal 6 (3) (2001) 334–342.

[11] J. A. White, N. Castelletto, H. A. Tchelepi, Block-partitioned solvers for coupled poromechanics: A unified framework, Computer Methods in Applied Mechanics and Engineering 303 (2016) 55–74.

[12] J. Kim, H. A. Tchelepi, R. Juanes, Stability, Accuracy, and Efficiency of Sequential Methods for Coupled Flow and Geomechanics, SPE Journal 16 (2) (2011) 249–262, sPE-119084-PA.

[13] F. Armero, J. C. Simo, A prior stability estimates and unconditionally stable product formula algorithms for nonlinear coupled thermoplasticity, International Journal of Plasticity 9 (1993) 749–782.

[14] F. Armero, Formulation and finite element implementation of a multiplicative model of coupled poro-plasticity at finite strains under fully saturated conditions, Computer Methods in Applied Mechanics and Engineering 171 (1999) 205–241.

[15] O. C. Zienkiewicz, D. K. Paul, A. H. C. Chan, Unconditionally stable staggered solution procedure for soil-pore fluid interaction problems, International Journal for Numerical Methods in Engineering 26 (5) (1988) 1039–1055.

[16] I. Romero, Thermodynamically consistent time-stepping algorithms for non-linear thermomechanical systems, International Journal for Numerical Methods in Engineering 79 (2009) 706–732.

[17] J. Kim, H. A. Tchelepi, R. Juanes, Stability and convergence of sequential methods for coupled flow and geomechanics: Drained and undrained splits, Computer Methods in Applied Mechanics and Engineering 200 (2011) 2094–2116.

[18] J. Kim, H. A. Tchelepi, R. Juanes, Stability and convergence of sequential methods for coupled flow and geomechanics: Fixed-stress and fixed-strain splits, Computer Methods in Applied Mechanics and Engineering 200 (2011) 1591–1606.

[19] A. Mikelic, M. Wheeler, Convergence of iterative coupling for coupled flow and geomechanics, Computational Geosciences 17 (3) (2013) 455–461.

[20] J. Kim, G. J. Moridis, D. Yang, J. Rutqvist, Numerical Studies on Two-way Coupled Fluid Flow and Geomechanics in Hydrate Deposits, SPE Journal 17 (2) (2012) 485–501.

[21] R. Liu, M. Wheeler, C. Dawson, R. Dean, Modeling of convection-dominated thermoporomechanics problems using incomplete interior penalty Galerkin method, Computer Methods in Applied Mechanics and Engineering 198 (2009) 912–919.

[22] O. Coussy, Mechanics of porous continua, John Wiley and Sons, Chichester, England, 1995.

[23] O. Coussy, Poromechanics, John Wiley and Sons, Chichester, England, 2004.

[24] J. C. Simo, T. J. R. Hughes, Computational inelasticity, Springer, Heidelberg, 1998.

[25] K. Aziz, A. Settari, Petroleum Reservoir Simulation, Elsevier, London, 1979.

[26] T. J. R. Hughes, The Finite Element Method: Linear Static and Dynamic Finite Element Analysis, Prentice-Hall, Englewood Cliffs, NJ, 1987.

[27] R. W. Lewis, Y. Sukirman, Finite element modelling of three-phase flow in deforming saturated oil reservoirs, International Journal for Numerical and Analytical Methods in Geomechanics 17 (1993) 577–598.

[28] R. W. Lewis, B. A. Schrefler, The finite element method in the static and dynamic deformation and consolidation of porous media, Wiley, Chichester, England, second edn., 1998.

[29] J. Wan, L. J. Durlofsky, T. J. R. Hughes, K. Aziz, Stabilized finite element methods for coupled geomechanic-sreservoir flow simulations, in: SPE Reservoir Simulation Symposium (SPE 79694), Houston, 3-5 Feb., 2003.

[30] A. J. White, R. I. Borja, Stabilized low-order finite elements for coupled solid-deformation/fluid-diffusion and their application to fault zone transients, Computer Methods in Applied Mechanics and Engineering 197 (2008) 43534366.

[31] P. A. Vermeer, A. Verruijt, An accuracy condition for consolidation by finite elements, International Journal for Numerical and Analytical Methods in Geomechanics 5 (1981) 1–14.

[32] M. A. Murad, A. F. D. Loula, Improved accuracy in finite element analysis of Biot's consolidation problem, Computer Methods in Applied Mechanics and Engineering 95 (1992) 359–382.

[33] J. Kim, H. A. Tchelepi, R. Juanes, Stability, accuracy, and efficiency of sequential methods for coupled flow and geomechanics, in: SPE Reservoir Simulation Symposium (SPE 119084), Woodland, 2-4 Feb., 2009.

[34] H. Yoon, J. Kim, Spatial stability for the monolithic and sequential methods with various space discretizations in poroelasticity, International Journal for Numerical Methods in Engineering 114 (694-718).

[35] J. Simo, Nonlinear stability of the time-discrete variational problem of evolution in nonlinear heat conduction, plasticity and viscoplasticity, Computer Methods in Applied Mechanics and Engineering 88 (1991) 111–131.

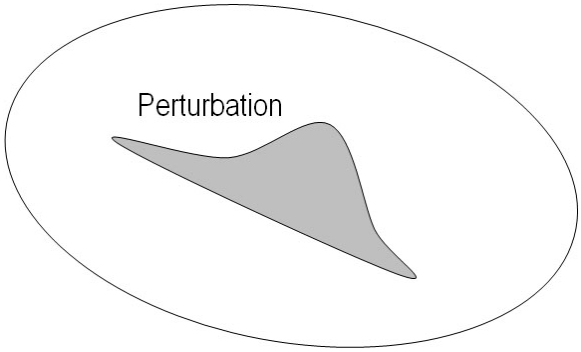

Figure 1: Perturbation introduced in the equilibrated domain. The perturbation can be considered as numerical errors.

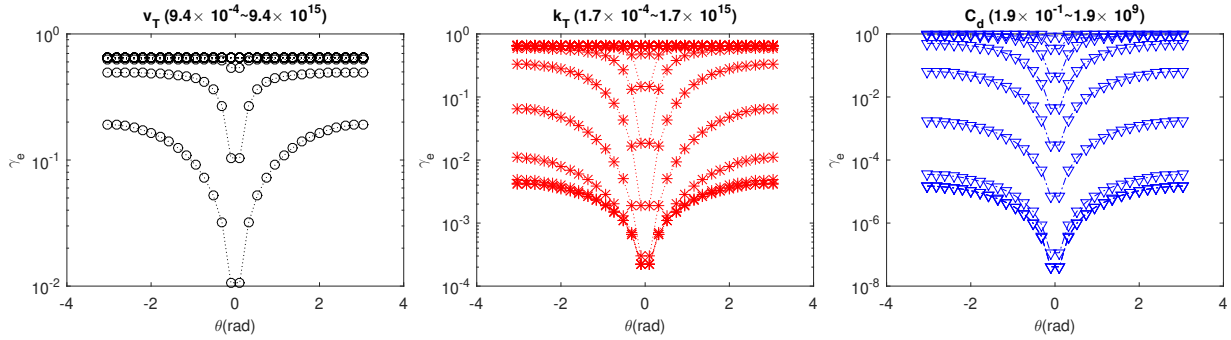

Figure 2: Distribution of the error amplification factor for various values of v_T/T_0, k_T, and C_d^*. The default values of Equation 54 are $T_0 = 298.15\ K\ (25\ ^oC)$, $k_p = 5.0 \times 10^{-15}\ m^2$, $k_T = 1.7\ Wm^{-1}K^{-1}$, $1/M = 1.32 \times 10^{10}\ Pa$, $\Delta x = 1.0\ m$, $\Delta t = 0.1\ s$, $C_d^* = 1.9\ kJ\ kg^{-1}\ K^{-2}$, $K_{dr} = 100\ MPa$, $\alpha_T = 10^{-3}\ K^{-1}$, $\alpha_M = 0.0$, $\alpha_\phi = 0.0$, $b = 1.0$, $v_f = 4.9 \times 10^{-6}\ m\ s^{-1}$, and $v_T/T_0 = 0.02 \times 10^{-5}\ kJ\ s^{-1}\ K^{-2}$. T_0 is a reference temperature in equilibrium.

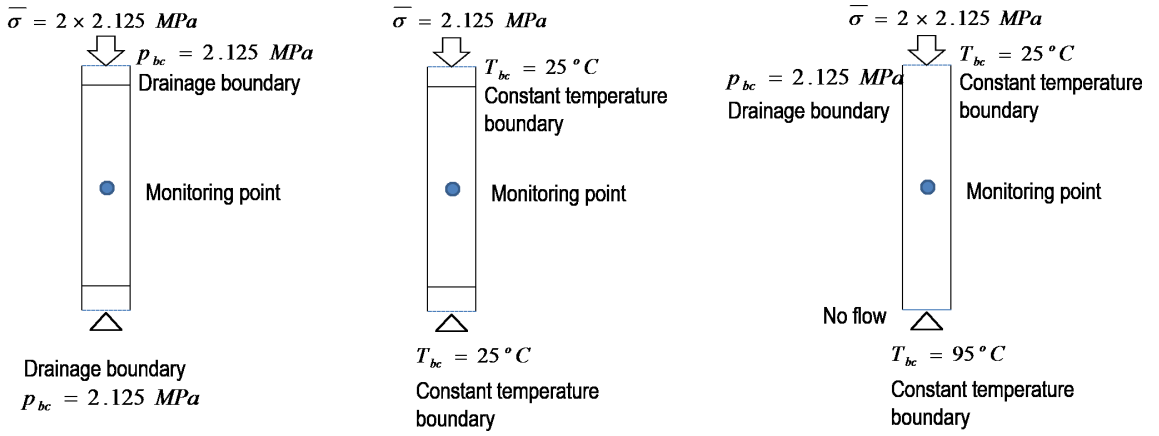

Figure 3: Schematics of 1D coupled fluid-heat-geomechanics problems. $(\cdot)_{bc}$ indicates the domain boundary. Left: isothermal consolidation of poromechanics (Case 1). Center: thermomechanics without changes in pressure (Case 2). Right: all-way coupled thermomechanics (Case 3).

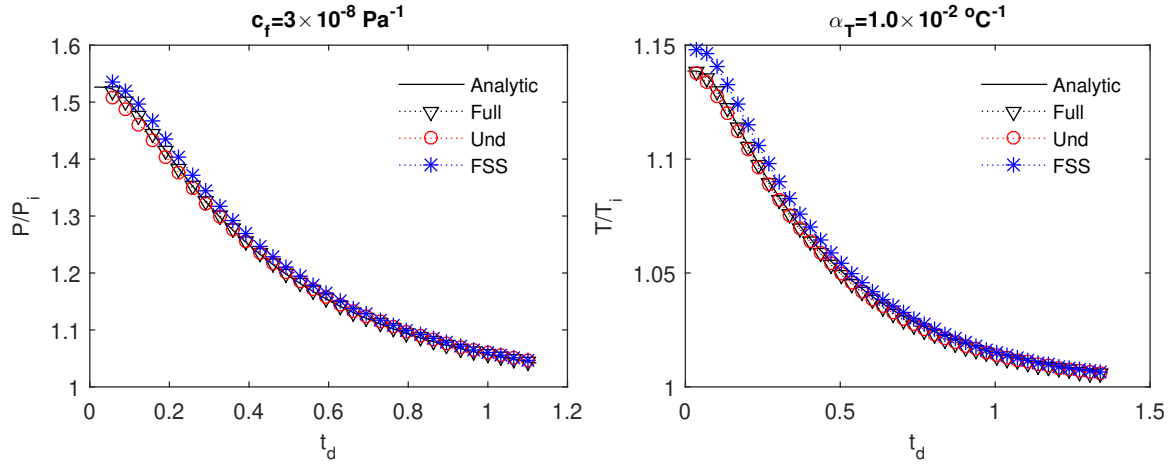

Figure 4: Verification test for the 1D thermoporomechanics. Left: isothermal poromechanics. Right: isobaric thermomechanics. The numerical results match the analytical solutions. 'Full','Und', 'FSS' indicate the fully-implicit, undrained-adiabatic, extended fixed-stress methods, respectively.

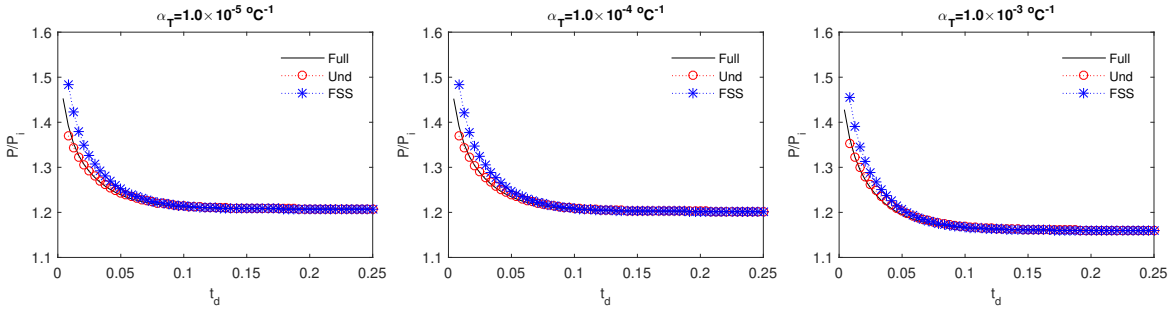

Figure 5: Pressure at the monitoring point for various α_T's. Pressure decreases due to thermal expansion of pore-volume, as α_T's increases.

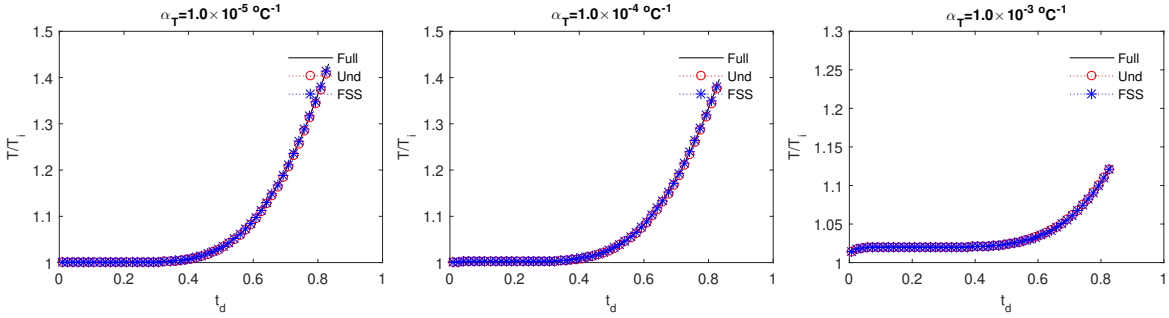

Figure 6: Temperature at the monitoring point for various α_T's. Deformation little affects changes in temperature for low α_T's. As α_T increases, thermal flow is retarded due to thermal dilation.

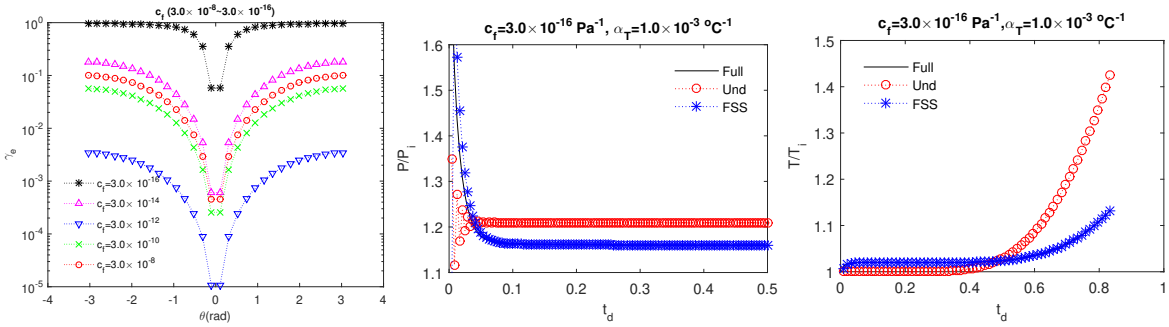

Figure 7: Left: Distribution of the error amplification factor for various values of fluid compressibility. Evolution of pressure (left) and temperature (right) at the monitoring point for incompressible fluid ($c_f = 3.0 \times 10^{-16}$). For incompressible fluid, the extended fixed-stress method still shows good accuracy while the undrained-adiabatic method is less accurate.

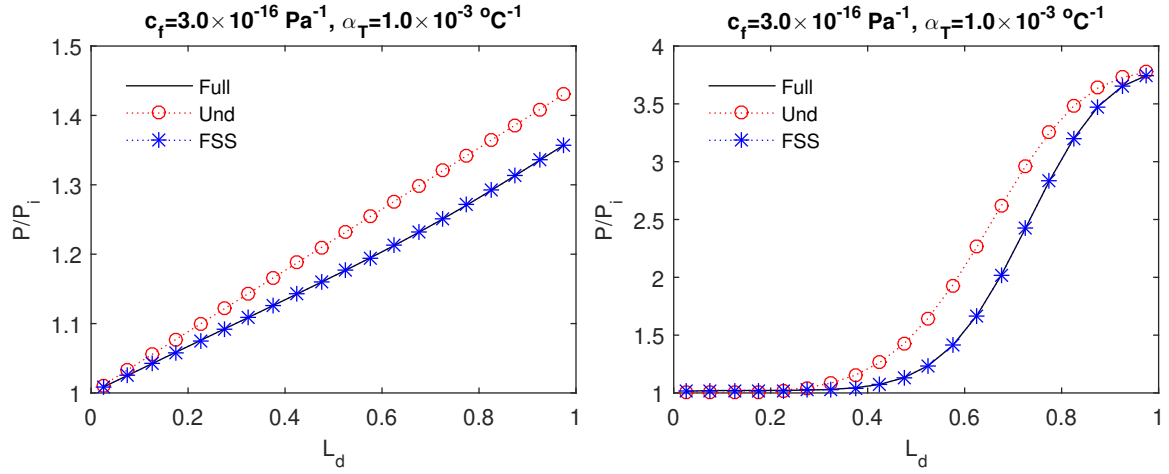

Figure 8: Distributions of pressure (left) and temperature (right) at $t_d = 0.83$. We identify good accuracy of the extended fixed-stress method.

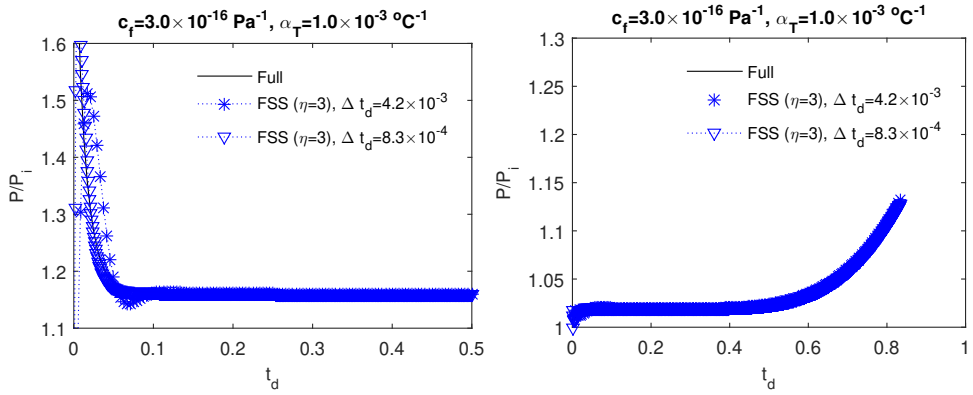

Figure 9: Evolution of pressure (left) and temperature (right) at the monitoring point with the extended fixed-stress method of $\eta = 3$, which still shows good accuracy.

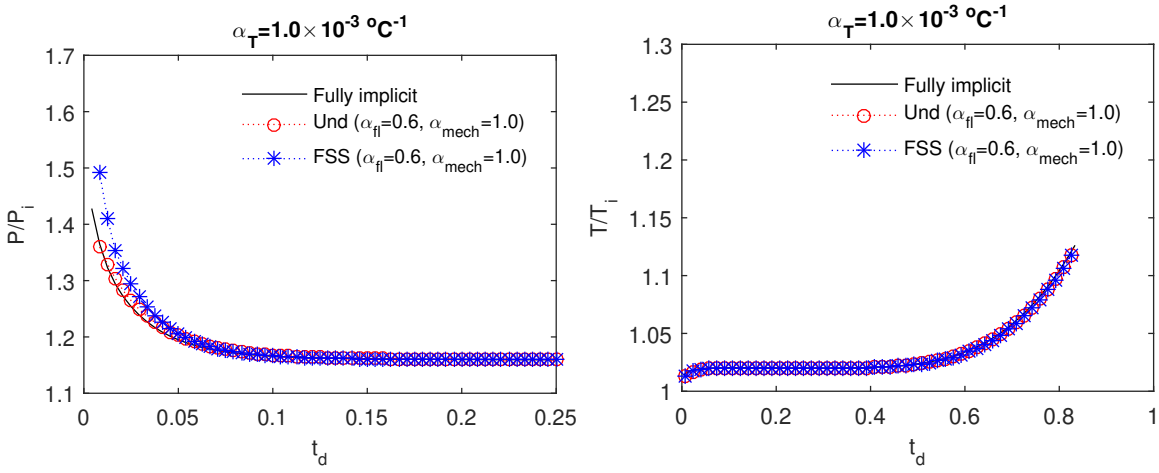

Figure 10: Mixed time stepping in the undrained-adiabatic and extended fixed-stress methods. Both sequential methods still provide stability and accuracy.